

VIRGO CLUSTER EARLY-TYPE DWARF GALAXIES WITH THE SLOAN DIGITAL SKY SURVEY. IV. THE COLOR-MAGNITUDE RELATION

THORSTEN LISKER^{1,2}, EVA K. GREBEL^{1,2}, AND BRUNO BINGGELI²

Accepted for publication by The Astronomical Journal

ABSTRACT

We present an analysis of the optical colors of 413 Virgo cluster early-type dwarf galaxies (dEs), based on Sloan Digital Sky Survey imaging data. Our study comprises (1) a comparison of the color-magnitude relation (CMR) of the different dE subclasses that we identified in Paper III of this series, (2) a comparison of the shape of the CMR in low and high-density regions, (3) an analysis of the scatter of the CMR, and (4) an interpretation of the observed colors with ages and metallicities from population synthesis models. We find that the CMRs of nucleated (dE(N)) and non-nucleated dEs (dE(nN)) are significantly different from each other, with similar colors at fainter magnitudes ($m_r \gtrsim 17$ mag), but increasingly redder colors of the dE(N)s at brighter magnitudes. We interpret this with older ages and/or higher metallicities of the brighter dE(N)s. The dEs with disk features have similar colors as the dE(N)s and seem to be only slightly younger and/or less metal-rich on average. Furthermore, we find a small but significant dependence of the CMR on local projected galaxy number density, consistently seen in all of $u-r$, $g-r$, and $g-i$, and weakly $i-z$. We deduce that a significant intrinsic color scatter of the CMR is present, even when allowing for a distance spread of our galaxies. No increase of the CMR scatter at fainter magnitudes is observed down to $m_r \approx 17$ mag ($M_r \approx -14$ mag). The color residuals, i.e., the offsets of the data points from the linear fit to the CMR, are clearly correlated with each other in all colors for the dE(N)s and for the full dE sample, implying that, at a given magnitude, a galaxy with an older stellar population than average typically also exhibits a higher metallicity than average. Given the observational data for Virgo dEs presented here and in the previous papers of this series, we conclude that there must be at least two different formation channels for early-type dwarfs in order to explain the heterogeneity of this class of galaxy.

Subject headings: galaxies: dwarf — galaxies: evolution — galaxies: stellar content — galaxies: fundamental parameters — galaxies: photometry — galaxies: clusters: individual (Virgo)

1. INTRODUCTION

It has long been known that a close correlation exists between the colors and luminosities of early-type galaxies, in the sense that more luminous objects have redder colors (e.g., Baum 1959; de Vaucouleurs 1961; Faber 1973; Sandage & Visvanathan 1978b; Caldwell 1983). A striking observation is the universality of the color-magnitude relation (CMR): it was found to be equal, within the measurement errors, for E and S0 galaxies within clusters, groups, or the field (Faber 1973; Sandage & Visvanathan 1978b,a; Bower et al. 1992), leading Faber (1973) to state that the colors of elliptical galaxies “are independent of all physical properties studied other than luminosity”. Faber also showed that a similar relation exists between the strength of spectral absorption features and luminosity, which basically is the spectroscopic analogue to the CMR. She interpreted the CMR as a trend of increasing metallicity with luminosity, which today is still considered to be the primary determinant of the CMR (e.g., Kodama & Arimoto 1997; Chang et al. 2006). This can be understood with a higher binding energy per unit mass of gas in more

massive galaxies, leading to stronger enrichment of the stellar populations. Recently, Bernardi et al. (2003) showed that color seems to correlate even more strongly with velocity dispersion than it does with luminosity. This implies that the CMR itself is most likely just a combination of the relation of luminosity and velocity dispersion (“Faber-Jackson relation”, Faber & Jackson 1976) and that of color and velocity dispersion. As Matković & Guzmán (2005) point out, the latter might hint at a more fundamental relation, namely between galaxy metallicity and mass.

While this trend includes the dEs, there has been disagreement about whether or not they follow the same CMR as the giant ellipticals. de Vaucouleurs (1961) found the dwarfs to be “systematically bluer” than the giants (but nevertheless following a CMR), whereas Caldwell (1983) reported a linear CMR over a range of $-15 \leq M_V \leq -23$ mag. However, his Figure 3 actually suggests that the slope of the CMR might indeed be slightly different for the dEs, in the same way as the results of de Vaucouleurs (1961) suggested (i.e., with decreasing magnitude, dwarfs become bluer more rapidly than giants do). Matković & Guzmán (2005) found a change in the slope of the Faber-Jackson relation for “faint early-type” galaxies — here, “faint” means $-17.3 \leq M_B \leq -20.5$ mag, thus reaching only slightly into the dwarf regime. De Rijcke et al. (2005) found an even larger difference in slope for a sam-

¹ Astronomisches Rechen-Institut, Centre for Astronomy of Heidelberg University (ZAH), Moenchhofstrasse 12-14, D-69120 Heidelberg, Germany

² Astronomical Institute, Dept. of Physics and Astronomy, University of Basel, Venusstrasse 7, CH-4102 Binningen, Switzerland
Electronic address: TL@x-astro.net

ple of 15 dEs, but argued that this is consistent with theoretical models, due to the dynamical response to starburst-induced mass loss, which is stronger for objects of lower mass. Significant constraints to such models could only be provided with a better understanding of dE formation. In contrast to giant ellipticals, formation mechanisms proposed for dEs in clusters are typically not based on an early formation epoch, but rather, on infall and subsequent transformation of late-type galaxies through gas-stripping and tidally enhanced star formation (e.g., Davies & Phillipps 1988; Moore et al. 1996; van Zee et al. 2004; Sabatini et al. 2005; Dellenbusch et al. 2007).

After having established a subdivision scheme of Virgo cluster early-type dwarf (dE) galaxies into subclasses with different shapes and distributions (Lisker et al. 2007, Paper III of this series), we can now proceed to the next logical step, namely to exploiting the wealth of data provided by the Sloan Digital Sky Survey (SDSS) Data Release 5 (DR5, Adelman-McCarthy et al. 2007) by a multicolor analysis of our sample of 413 dEs. However, the colors of different dEs, or of dEs of different subclasses, can not straightforwardly be compared with each other: the existence of the CMR requires such a comparison to be done either at fixed magnitude or with a correction for magnitude differences. For this reason, we shall explore the dE colors mainly through an analysis of their CMR.

One would naively expect that, if two given dE subclasses formed through different mechanisms, their resulting CMRs should display differences as well, since the relation of galaxy mass to the properties of its stellar population should depend to some extent on how and when the latter was formed. On the other hand, the apparent universality of the CMR – mainly defined for giant ellipticals – would seem to argue against such differences. Conselice et al. (2003) found considerable scatter of the CMR of dEs in the Perseus cluster at magnitudes $M_B \geq -15$ mag, apparently caused by two different sequences of dwarfs in color-magnitude space. They argue that the early-type dwarfs must have multiple origins – similar to the conclusion of Poggianti et al. (2001) about an apparent bimodal metallicity distribution of Coma cluster dwarfs that might hint at more than one formation channel. We should be able to test the presence of such a bimodality in more detail, given our “preparatory work”, namely the separation of dE subclasses that have different shapes and distributions (Paper III). Moreover, the SDSS multicolor data enable us to construct CMRs in more than one color, and also to analyze our galaxies in color-color space, thereby translating colors into ages and metallicities. Since Rakos & Schombert (2004) found the dE(nN)s in the Coma and Fornax clusters to be younger and to have a higher metallicity than the dE(N)s, we can perform a similar analysis for our Virgo cluster galaxies, allowing us to test the similarity of dE populations of different clusters.

2. DATA

The SDSS DR5 covers all galaxies listed in the Virgo cluster catalog (VCC, Binggeli et al. 1985), except for an approximately $2^\circ \times 2.5^\circ$ area at $\alpha \approx 186^\circ 2$, $\delta \approx +5^\circ 0$. It provides reduced images taken in the u , g , r , i , and z bands with an effective exposure time of 54s in each

band (see also Stoughton et al. 2002), as well as the necessary parameters to flux-calibrate them. The pixel scale of $0''.396$ corresponds to a physical size of 30 pc at our adopted Virgo cluster distance of $d = 15.85$ Mpc (distance modulus $m - M = 31.0$ mag; van den Bergh 1996; Graham et al. 1999), which we use throughout.

The SDSS imaging camera (Gunn et al. 1998) takes data in drift-scanning mode nearly simultaneously in the five photometric bands, and thus combines very homogeneous multicolor photometry with large area coverage and sufficient depth to enable a systematic analysis of dEs. The images have an absolute astrometric accuracy of $\text{rms} \leq 0''.1$ per coordinate, and a relative accuracy between the r band and each of the other bands of less than 0.1 pixels (Pier et al. 2003). They can thus easily be aligned using their astrometric calibration and need not be registered manually. Furthermore, adjacent SDSS images can be accurately combined, allowing the extraction of subimages that fully cover a given object, even if the latter lies at the edge of an SDSS image.

The rms of the noise per pixel corresponds to a surface brightness of approximately 24.2 mag arcsec $^{-2}$ in the u band, 24.7 in g , 24.4 in r , 23.9 in i , and 22.4 in z . The typical total signal-to-noise ratio (S/N) of a bright dE ($m_B \approx 14$ mag) amounts to about 1000 in r , within an aperture radius of approximately two half-light radii. For a faint dE ($m_B \approx 18$ mag) this value is typically about 50. While the S/N in g and i is similar, it is several times lower in z and almost ten times lower in u .

Since the sky level on the SDSS images can vary by some tenths of the noise level across an image, it is not sufficient to subtract only a single sky flux value from each image. We therefore determined the sky flux distribution across a given image using a thorough procedure, as described in detail in Paper III. The sky-subtracted images were then flux-calibrated and corrected for Galactic extinction (Schlegel et al. 1998). We also correct for the reported³ SDSS zeropoint offsets in u and z from the AB system (Oke & Gunn 1983):

$$u_{\text{AB}} = u_{\text{SDSS}} - 0.04 \text{ mag} \quad (1)$$

$$z_{\text{AB}} = z_{\text{SDSS}} + 0.02 \text{ mag} \quad (2)$$

3. SAMPLE AND BASIC MEASUREMENTS

Our working sample of Virgo cluster dEs contains 413 certain cluster members that were initially classified as early-type dwarfs in the VCC (“dE” or “dS0”, including uncertain candidates), that are brighter than $m_B \leq 18.0$ mag, that passed our visual examination for confusion with possible dwarf irregulars, and for which a Petrosian radius (Petrosian 1976) could be derived. The details of our sample selection are described in Paper III.

For each galaxy, we determined a “Petrosian semimajor axis” (hereafter Petrosian SMA, a_p), i.e., we use ellipses instead of circles in the calculation of the Petrosian radius (see, e.g., Lotz et al. 2004b). The total flux in the r band was measured within $a = 2 a_p$, yielding a value for the half-light semimajor axis, $a_{\text{hl},r}$. Axial ratio and position angle were then determined through an isophotal fit at $a = 2 a_{\text{hl},r}$. The details of this process are outlined in Paper III. Disturbing foreground or background objects were properly masked, and the area blocked by

³ See <http://www.sdss.org/dr5/algorithms/fluxcal.html>

these masks was taken into account in the determination of the total r -band flux. We also decided to mask the nuclei, if present, in order to guarantee that a nucleus with a different color than its host galaxy would not affect our measurements of the inner galaxy colors. For each galaxy and band, we measured the flux within three elliptical apertures: $a \leq 0.5 a_{\text{hl},r}$ (“small aperture”), $a \leq a_{\text{hl},r}$ (“intermediate aperture” or half-light aperture), and $a \leq 2 a_{\text{hl},r}$ (“large aperture”).

4. ERROR ESTIMATION

The actual errors on the measured fluxes are a combination from several different sources of uncertainties, which we attempt to estimate as realistically as possible. The noise level in every image is measured as the standard deviation around the mean of all unmasked pixels, clipped five times iteratively at 3σ . For each galaxy, band, and aperture, we then adopt the following uncertainties of a given flux measurement:

- The “S/N uncertainty” is the inverse S/N value.
- The “sky level uncertainty” is derived from the uncertainty in the sky level determination per pixel, which is taken to be 0.2% of the noise level: the mean flux value of all unmasked pixels after sky subtraction typically deviates from zero by this value or less.
- The uncertainty in the determination of the Petrosian SMA (“Petrosian uncertainty”) is estimated to be of the same order as the sky level uncertainty, which we therefore simply count twice in our calculation of total errors. We elaborate on this uncertainty in more detail in Appendix A.
- The uncertainty in the photometric calibration (“calibration uncertainty”) is reported³ as 0.02 mag in g , r , and i , and 0.03 mag in u and z .
- The natural red leak of the u filter causes the “ u -leak uncertainty” of 0.02 mag³.

For each flux measurement f_x in a given band x , we combine all the different uncertainties to a single uncertainty Δf_x . This is done by adding the individual uncertainties quadratically, as exemplified below for the u band.

$$\Delta f_u = \left(\left(\frac{\sigma_u \cdot \sqrt{N_{\text{pix}}}}{f_u} \right)^2 + 2 \cdot \left(\frac{0.002 \sigma_u \cdot N_{\text{pix}}}{f_u} \right)^2 + (10^{0.4 \cdot 0.03} - 1)^2 + (10^{0.4 \cdot 0.02} - 1)^2 \right)^{0.5} \quad (3)$$

Here, σ_u denotes the noise level per pixel, as described above. N_{pix} is the number of pixels included in the given aperture. The first term is the S/N uncertainty, the second term is the combination of sky level uncertainty and Petrosian uncertainty, and the last two terms are the calibration uncertainty and the u -leak uncertainty, respectively.

Errors on measured color values are calculated by adding the relative flux errors from each band quadratically, and converting them to magnitudes. An example is given below for the $u - g$ color error, $\Delta(u - g)$, calculated from the u band flux f_u , the g band flux f_g , and

their respective errors.

$$\Delta(u - g) = -2.5 \log \left(1 - \sqrt{\left(\frac{\Delta f_u}{f_u} \right)^2 + \left(\frac{\Delta f_g}{f_g} \right)^2} \right) \quad (4)$$

Equation 4 would actually yield only the errors on one side, whereas the errors on the other side would be calculated from $-2.5 \log(1 + \sqrt{\dots})$, and would consequently be smaller. However, we prefer the conservative approach to use the larger errors for both sides. Galaxies for which the relative flux error becomes ≥ 1 are excluded from the respective diagrams or calculations, since the argument to the logarithm in Equation 4 would become ≤ 0 , denoting an uncertainty that is too large to be useful. This occurs only for five of the fainter objects, for colors that include the u band.

5. STATISTICAL TECHNIQUES

5.1. Linear fitting of color-magnitude relations

Since color-magnitude relations of early-type galaxies are found to be linear or nearly linear (e.g., Bower et al. 1992; Bernardi et al. 2003) we describe our relations by fitting a straight line to the data points. A common approach is least-squares fitting, which, however, can sometimes lead to undesired results, e.g., a “best fit” with a slope that differs significantly from that defined by the bulk of data points (Press et al. 2002, see their Figure 15.7.1). We therefore prefer to apply a robust fitting technique using a so-called M-estimate (Press et al. 2002), namely the mean *absolute* deviation (rather than the mean square deviation used for least-squares fitting). See, e.g., Chang et al. (2006) for an earlier application of this technique to color-magnitude relations.

We thus have to minimize the function

$$\mu(a, b) = \sum_{i=0}^{N-1} \left| \frac{c_i - a - b \cdot m_i}{\sigma_i} \right| \quad (5)$$

where a and b are the zeropoint and the slope of the relation, respectively, m_i and c_i are magnitude and color of the i -th galaxy, and σ_i is the corresponding measurement uncertainty, or alternatively, any kind of inverse weight. We set σ_i equal to the respective color error, neglecting magnitude errors, since they are small compared to the range of magnitudes that is considered (compare, e.g., Figure 1), and since they are also closely correlated with the color errors. For some cases we tested $\sigma_i = \sqrt{(\Delta m_i)^2 + (\Delta c_i)^2}$, i.e., quadratically adding magnitude and color error. We found no significant differences in the resulting best fit. The fitting process is repeated two times iteratively, excluding data points that are offset from the fitted line by more than three times the derived rms scatter.

5.2. Statistical comparisons of color-magnitude relations

In the following sections, we aim at performing *quantitative*, statistical comparisons of two given color-magnitude relations. Here, we briefly outline our method for such a comparison, and present a more detailed description in Appendix B.

We decided on an approach that takes into account both the data points themselves and the linear fits to them. For two given sets of data points A and B, we

compute the color residuals of both sets about the CMR A and statistically compare these residuals through a K-S test and a Student’s t-test for unequal variances. This is done analogously for the residuals about the CMR B. The final probability for a common underlying distribution from the two K-S tests is then derived by averaging both values of the K-S statistic D (see Press et al. 2002). The final probability from the two t-tests is adopted to be the larger of the two individual probabilities.

In the course of the paper, we will usually simply refer to the higher of the probabilities from the K-S test and the t-test. We typically consider two CMRs to be “significantly” different if the statistical comparison yields probabilities below a few percent.

6. COLOR-MAGNITUDE RELATIONS OF EARLY-TYPE DWARF SUBCLASSES

In Paper III we established a subdivision scheme for the dEs that comprises several subclasses with different properties: dEs with disk features like spiral arms or bars (dE(di)s, Lisker et al. 2006a, Paper I), dEs with blue centers (dE(bc)s, Lisker et al. 2006b, Paper II) caused by recent or ongoing central star formation, bright and faint ordinary dEs (i.e., not displaying disk substructure or a blue center) that are nucleated (dE(N)s), and bright and faint ordinary dEs that have no nucleus or only a weak nucleus that is below the detection limit of the VCC (dE(nN)s). The bright dE(nN)s, dE(di)s, and dE(bc)s are shaped like thick disks and show no central clustering, while the faint dE(nN)s and the dE(N)s have rounder shapes, and the dE(N)s are more strongly concentrated towards the cluster center. These results define a morphology-density relation *within* the dE class, and we now seek to investigate whether this is also correlated with color.

In Figure 1 we present the relations of color and r magnitude separately for dE(N)s, dE(nN)s, dE(di)s, and dE(bc)s, as well as for the full dE sample excluding dE(bc)s. Our choice of presented colors relies partly on the considerations outlined in Section 9.1: $u-r$ is mainly age-sensitive, $i-z$ is metallicity-sensitive, $g-i$ provides the largest wavelength baseline within the three high-S/N SDSS bands (g , r , i), and $g-r$ is an alternative to $u-r$, since the smaller wavelength range of $g-r$ is counterbalanced by the significantly smaller errors in g as compared to u . The horizontal dotted lines denote the separation between our bright and faint subsamples, which were divided at the median r brightness of our full sample, $m_r = 15.67$ mag (Paper III; corresponding to $M_r = -15.33$ when adopting $m-M = 31.0$). The CMRs of the dE subclasses are compared to each other in the lowermost row of the figure.

The resulting parameters of the corresponding linear fits are given in Table 1. While the colors presented in Figure 1 were measured within the half-light aperture (as defined in Section 3), Table 1 also includes the CMR-parameters for the small and large apertures. These will be taken into account in Section 9.2, where systematic radial stellar population gradients will be discussed.

First, we focus on the dE(bc)s. From Paper II, we expect that the colors beyond $a > 0.5 a_{\text{hl},r}$ are on average only slightly affected by the positive central color gradient, and that the colors are not noticeably affected beyond $a > a_{\text{hl},r}$. However, in all of $u-r$, $g-r$, and

$g-i$, the dE(bc)s are somewhat bluer than the other dE subclasses. Note that no precise statements can be made about the slope of their CMR, since it is constrained at the faint end by only two data points. Nevertheless, it can be seen that the scatter in $g-r$ and $g-i$ is somewhat larger than that of the other subclasses at the same magnitudes. This is confirmed by the respective values of the rms scatter, which are larger by a factor of ~ 1.5 for the dE(bc)s. In contrast, the dE(bc)s follow a surprisingly tight relation in $i-z$: the scatter is a factor of two lower than the rms of the measurement errors⁴ (see Table 1), and likewise, it is lower than the scatter of all other subclasses in this bin. At larger radii, the relation seems to turn around, i.e., such that brighter galaxies are bluer, but again, the small sample size does not allow robust conclusions. Nevertheless, a trend for the CMR to turn around is also seen for the dE(N)s and the dE(nN)s.

The CMR of the dE(di)s is similar to that of the dE(N)s in all of $u-r$, $g-r$, and $g-i$, although it is always slightly bluer. According to our statistical tests, as described in Section 5.2 and presented in Table 2, this small difference is nevertheless significant in $g-i$: for all apertures, the probability of a common underlying distribution function⁵ with the dE(N)s is $\leq 1.6\%$. For the small and intermediate apertures of $g-r$, it is $\leq 2.3\%$, and for the small aperture of $u-r$ it is $\leq 1.7\%$. We note, though, that these values should be taken with a grain of salt, since the linear fit to the dE(di)s is constrained by only three data points at the faint end, and since the sample is of only moderate size. Nevertheless, the slight blueward offset of the dE(di)s from the dE(N)s is consistently seen in all the above bands. In $i-z$, however, the dE(di)s basically follow the same relation as the dE(N)s. For the large aperture, the dE(di)s are slightly redder, but the difference is not significant (see Table 2).

The dE(nN)s follow a steeper CMR than the dE(N)s or the dE(di)s in all colors and apertures, including $i-z$ even though the difference is small there. They lie at about the same color values at the faint end of the sample, but become red less rapidly with increasing magnitude. The difference between the CMRs of the dE(nN)s and the dE(N)s is significant in all apertures of $g-r$ (probability of common distribution $\leq 0.5\%$) and $g-i$ (0.0%). It is, however, not significant in $i-z$ ($\geq 15\%$), and hardly significant in $u-r$ ($\leq 9\%$). To illustrate these differences in a more obvious way than Figure 1 does, we overplot in Figure 2 the linear fit of the respective *other* subclass over the data points of dE(N)s and dE(nN)s — the discrepancy in $g-r$ and $g-i$ is clearly seen.

In order to further quantify the above considerations, one would want to compare average color values of the subsamples. The problem with this approach is that the samples are not distributed equally in magnitude; the average colors could thus come out different just because of the existence of a color-magnitude relation. Therefore, we compare instead the color values of the linear fits to the CMRs at a fixed magnitude. We choose two

⁴ This, along with the tight relation of the dE(di)s, confirms that we did not underestimate our photometric errors

⁵ While we always consider the probabilities from both the K-S test and the t-test, we recall that the t-test compares the *means* of the residuals about the CMR, not the distributions themselves. For simplicity, though, we shall continue speaking of the “probability of a common underlying distribution”.

magnitude values for this comparison, namely the median r magnitude of our bright dEs, $m_{r,\text{bri.}} = 14.77$ mag ($M_{r,\text{bri.}} = -16.23$) and the median r magnitude of our faint dEs, $m_{r,\text{fai.}} = 16.51$ mag ($M_{r,\text{fai.}} = -14.49$), which we refer to hereafter as the bright and faint “reference magnitude”, respectively. The corresponding color values for the different subclasses are given in Table 3.

The values so derived reflect our above comparisons of the various CMRs: the dE(N)s are redder than the dE(nN)s in $u-r$, $g-r$, and $g-i$ at both the bright and the faint reference magnitudes, with the difference being smaller for the latter. In $i-z$, the dE(N)s are still redder at the bright reference magnitude, whereas no clear difference is present at the faint reference magnitude, also given the rather large scatter of the CMR. The dE(di)s, which we consider only at the bright reference magnitude, are intermediate between the dE(nN)s and the dE(N)s in $u-r$, $g-r$, and $g-i$. In $i-z$, their colors are very similar to those of the dE(N)s, again reflecting our above analysis of the CMRs. In Section 9, we will attempt to interpret these color values in terms of age and/or metallicity differences.

We need to point out one possible caveat with the above comparisons: in Paper III we found significant differences in both the shapes and the distributions of faint and bright dE(nN)s. It might thus be not appropriate to fit a single line through their combined sample. Therefore, we show in Figure 3 separate fits to the CMRs of the bright and faint dEnN subsamples. While these do differ from the fit to the full sample, they are rather poorly constrained: the range in magnitude covered by each subsample is not very large compared with the scatter of the data points. The linear fits might thus be not reliable enough to allow a robust statistical comparison. Nevertheless, a comparison with a similar fit to the bright subsample of the dE(N)s shows that the bright dE(nN)s are still significantly bluer than the (bright) dE(N)s in $u-r$, $g-r$, and $g-i$ at the bright reference magnitude (see the two rightmost columns of Table 3).

7. COLOR-MAGNITUDE RELATIONS OF DENSITY-SELECTED SAMPLES

A weak dependence of the stellar population ages of early-type galaxies on local environmental density has recently been reported by Bernardi et al. (2006), based on a study of Lick indices. These authors found early-type galaxies in high-density environments to be slightly older than at lower densities. Our large sample size allows us to test whether this is the case for dEs as well — we can of course only probe a cluster environment, but the range in local densities (see, e.g., Paper III) should be large enough to find such an effect, if present.

We thus subdivide the sample of dE(N)s, dE(nN)s, and our full dE sample (excluding dE(bc)s) at their respective median local projected densities. These are, in units of the logarithm of the number of galaxies per square degree, 1.374 for the dE(N)s, 1.198 for the dE(nN)s, and 1.293 for the full dE sample. It can be seen from these values that the dE(N)s populate on average regions of higher density than the other subclasses, reflecting their centrally clustered spatial distribution, which is not seen for the other subclasses (Paper III). As described in the previous papers of this series, local projected density is calculated by defining a circular area around each galaxy

that includes its ten nearest neighbour cluster members, independent of galaxy type (Dressler 1980; Binggeli et al. 1987).

The resulting CMRs are shown in Figures 4 and 5. The respective subsamples are denoted by a subscript “low” for the low-density subsample, and “high” for the high-density subsample. The pairwise statistical comparisons of the CMRs of low and high-density subsamples are given in Table 4.

For all colors of $u-r$, $g-r$, and $g-i$, the dE(N)s, dE(nN)s, and the full dE sample, the derived CMR at lower densities is consistently steeper than at higher densities. Typically, the CMRs intersect at the fainter magnitudes of our sample, and with increasing magnitude, galaxies are on average redder in the high-density regime. In $i-z$, the low-density subsamples also follow a slightly steeper CMR, but the intersection occurs at brighter magnitudes. Note that, typically, any correlation with *projected* density would be even stronger with true *volume* density, since projection always causes some objects to apparently lie close to the center that are actually situated in front of or behind the center.

The difference between the low and high-density subsamples of our full dE sample is significant in $u-r$ (probabilities for a common underlying distribution $\leq 3.0\%$ for all apertures, see Table 4), and even more significant in $g-r$ ($\leq 0.9\%$ for all apertures) and $g-i$ (0.0% for all apertures). The dE(N)s alone also display significant differences between the two density regimes, namely for the intermediate apertures in $u-r$ (probability $\leq 2.0\%$) and $g-i$ ($\leq 2.2\%$). In $g-r$, the probability is still lower than 6.5% . The fact that the percentages are not as low as for the full dE sample, and that significant differences are not found for all apertures, is at least partly due to the lower sample size as compared to the full sample. Although a density difference is also seen for the dE(nN)s in Figure 4, it is not statistically significant: the lowest probabilities for a common distribution occur in $g-i$ for the small aperture ($\leq 6.7\%$) and the intermediate aperture ($\leq 10.2\%$). Here, probably the subsample sizes are too small and the scatter of the CMRs too large for the rather small differences to be significant.

The dE(N)s and dE(nN)s are populating different density regimes (Paper III) and display significantly different CMRs (see Section 6). Therefore, one might conjecture that the difference between the density-selected subsamples of the *full* dE sample stems mainly from the difference between the two subclasses. The fact that the dE(N)s alone also show significant density differences would argue against this hypothesis, but we nevertheless conduct a further test. We first construct a “combined sample”, which differs from the full sample in that it contains no dE(di)s. Its median local projected density is 1.295, and divides the sample into halves that, initially, do *not* contain an equal number of dE(N)s and dE(nN)s. For the low (high) density half of the combined sample, we then exclude randomly that many dE(nN)s (dE(N)s) that the number of galaxies belonging to each subclass becomes equal. This leads to a combined sample containing 86 objects of each subclass in the low-density part, and 55 in the high-density part, adding up to 282 objects in total. This approach guarantees that differences between the resulting low- and high-density CMRs cannot be caused by one of the subclasses dominating over the

other in one density regime.

The random exclusion of galaxies is repeated 100 times, and the resulting CMRs are compared as previously described. We use the intermediate aperture of $g-i$, where the density difference was found to be significant for the dE(N)s alone (210 objects). The probability for a common distribution has a median value of 1.2% among our 100 realizations and exceeds 5% in 11 cases and 10% in 3 cases only. This confirms that a density dependence of the CMR is present and is not faked by an unequal combination of dE(N)s and dE(nN)s. Nevertheless, the illustration of the first 8 realizations in Figure 6 also leave room to speculate whether it is actually only the brighter dEs whose color depends on density (and is reddest in high-density regions), thereby affecting the fit to the CMR of all dEs. A further subdivision of the dEs into bright and faint subsamples, in addition to the subdivision by density, yields significant differences for the bright part of the full dE sample in all of $u-r$, $g-r$, and $g-i$ ($\leq 2.4\%$ for all colors and apertures). Still, at least for the small and intermediate apertures in $g-i$, the statistical comparison also yields a significant difference for the faint subsample ($\leq 1.8\%$). Among the dE(N)s and dE(nN)s, the lowest probability is the one for the bright dE(N)s in $g-i$ for the small aperture, with $\leq 6.6\%$. An even larger sample size would be required to draw reliable conclusions on the precise cause of the correlation between CMR and density.

So far, we did not consider the possibility that the density dependence of the CMR could be caused by different average distances of the subsamples along the line of sight. To test this, we consider the low and high-density subsample of all dEs (excluding dE(bc)s) in $g-i$. At the color value that the CMR of the high-density subsample has at the bright reference magnitude, the CMR of the low-density subsample is 0.62 mag brighter. Assuming an average distance modulus of $m-M = 31.0$ mag, this would correspond to an average offset of the subsamples along the line of sight of 4.5 Mpc. Moreover, both CMRs intersect at the fainter magnitudes – thus, the brighter dEs that are in regions of higher projected density would have to be, *on average*, 4.5 Mpc closer to us than the fainter dEs in the same projected regions.

A difference in distance modulus of 1.0 mag between the Virgo cluster parts termed “cluster A” (i.e., basically the part of the cluster that has a declination $\delta \gtrsim 10^\circ$, see Binggeli et al. 1993) and the western part of “cluster B” (southward of cluster A and within a circular region around M 49) was reported by Gavazzi et al. (1999), such that the latter part would be further away by 8.6 Mpc. Their study is based on a combined sample of early-type and late-type galaxies. While the number of dEs in this rather small region appears to be too low to account for the differences that we see in the CMRs, we nevertheless test this possibility by excluding all galaxies below a declination $\delta < 10^\circ$. However, the difference between the low and high-density CMR is still equally large. Within cluster A, Gavazzi et al. (1999) give a dispersion of 0.45 mag in their determination of the distance modulus — but they note that this value is comparable to the nominal uncertainty in the methods used. Based on the surface brightness fluctuations of 16 Virgo dEs, Jerjen et al. (2004) found a distance dispersion of ± 1.45 Mpc, too low to be able to explain the observed

differences. While their result is derived from a rather small sample, they noted that this dispersion, compared to the tangential extension of the cluster, implies a prolate spatial distribution of the galaxies that excellently agrees with other studies (Nielsen & Tsvetanov 2000; West & Blakeslee 2000). We also point out again that the color differences would require a *systematic offset* of 4.5 Mpc, not just a distance dispersion. Furthermore, such an offset should also be reflected in the magnitude distribution of the two subsamples — yet their median r magnitudes differ by 0.07 mag only, and their distributions are very similar. From these considerations, it is clear that the significant correlation of the CMR with local density is real and can not be explained with differences in distance.

8. THE SCATTER OF THE COLOR-MAGNITUDE RELATION

If the observed scatter of the CMR would be solely due to measurement uncertainties, no correlation should be present between the color residuals in two different colors — except, obviously, for colors that share a certain band, like $u-r$ and $g-r$. If, on the other hand, a significant true scatter was present (like, e.g., found by Conselice et al. (2002) for early-type dwarfs in the Perseus cluster), one would expect at least some correlation between the residuals: a dE that is intrinsically bluer in $u-r$ than most of the other galaxies should typically not be intrinsically redder in $g-i$ than most other dEs, since the wavelength ranges covered by these colors overlap significantly. (It would, though, be “allowed” to be redder in $i-z$.) Likewise, if the scatter was due to a spread in distance and therefore in magnitude, most galaxies would fall on the same side of the CMR in all colors.

We therefore present in Figure 7 a pairwise comparison of the color residuals for $u-r$ vs. $g-i$, $u-r$ vs. $i-z$, and $g-r$ vs. $i-z$. In each quadrant of each figure panel, we give the percentage of objects that falls within it as black numbers. A correlation is clearly seen for the dE(N)s and for the full dE sample in $u-r$ vs. $g-i$, for which more than twice as many objects lie within the upper right and lower left quadrant than within the other two. In $u-r$ vs. $i-z$, the correlation is somewhat weaker, and again slightly weaker in $g-r$ vs. $i-z$. For the dE(nN)s, only $u-r$ vs. $g-i$ shows a clear correlation. These results indicate that there must be a significant true scatter of the CMR, similar to the results of Secker et al. (1997) for the Coma cluster.

Appendix C describes in more detail how we arrive at the above conclusions. There, we also calculate that the distance modulus dispersion of our galaxies would have to be ± 0.61 mag if it were the sole cause of the observed correlation. However, the value measured by Jerjen et al. (2004) is only ± 0.177 mag. Therefore, while a certain distance scatter is naturally unavoidable, we conclude that a significant *intrinsic* color scatter must be present for our galaxies, with a strong correlation between the different colors.

A further question that can be addressed with our data is whether the scatter of the CMR increases with decreasing luminosity. For example, Conselice et al. (2002, 2003) found a significant increase of the CMR scatter of early-type galaxies at magnitudes $M_B \gtrsim -15$, roughly corresponding to $M_r \gtrsim -16$ and thus to $m_r \gtrsim 15$. In

order to quantify how the scatter changes with magnitude in our data, we show in Figure 8 the ratio of the rms of the color residuals about the CMR to the rms of the color errors, binned to quartiles defined by the r brightnesses of our full sample (i.e., the four bins are separated at the previously defined bright reference magnitude, $m_{r,\text{bri.}} = 14.77$, the median value, $m_r = 15.67$, and the faint reference magnitude, $m_{r,\text{fai.}} = 16.51$ mag). We use this “rms-ratio” in order to detect any *real* change in the scatter, i.e., one that is not caused only by increasing measurement errors at fainter magnitudes. The values shown were derived using the half-light aperture.

As can be seen from Figure 8, neither the dE(N)s, the dE(nN)s, nor the full dE sample shows an increase in the CMR scatter at fainter magnitudes in any color. In contrast, the scatter increases in $u - r$ with *increasing* brightness, and also does so in $g - i$ for the *brightest* bin of the dE(N)s. A trend for the latter is also seen for the dE(nN)s in $g - i$: the second-brightest bin shows an increase, but the brightest bin contains too few objects to be reliable. These variations in the scatter can actually be seen qualitatively in Figure 1, in particular the large scatter of the bright dE(N)s in $g - i$. We can only speculate that this could be caused by a larger spread in the stellar population properties of these objects, and that it might be in some way related to the potential break in dwarf galaxy structure discussed by Binggeli & Cameron (1991) at $M_{B_T} \simeq -16$. This magnitude corresponds to $m_B = 15.7$ given their $m - M = 31.7$, and is thus roughly equivalent to $m_r = 14.7$. We can certainly rule out a significant increase in the color scatter of the Virgo cluster dEs about the CMR down to $m_r \approx 17$ mag (below which our sampling becomes more sparse), i.e. $M_r \approx -14$ mag, in contrast to what Conselice et al. (2003) observed for early-type dwarfs in the Perseus cluster.

We further note that the overall scatter of the dE(nN)s is clearly larger than that of the dE(N)s in all colors except $i - z$ (Figure 8), again confirming the qualitative impression from Figure 1. For this, there might be a simple explanation: the color scatter of a sample of galaxies with a given spread in stellar population age will decrease with time. This can be illustrated using synthetic colors of a model stellar population that formed in a single exponentially declining ($\tau = 1$ Gyr) peak of star formation, derived from population synthesis models of Bruzual & Charlot (2003) with a metallicity of $[\text{Fe}/\text{H}] = -0.64$ (see Section 9). We now consider the change in $g - i$ color of this stellar population during 3-Gyr intervals from an age of 1.5 Gyr to 13.5 Gyr (our adopted look-back time to the first star formation in the Universe, see Section 9.1). In the first interval, i.e., from 1.5 to 4.5 Gyr, the $g - i$ color reddens by 0.48 mag. In the next three intervals, it reddens by only 0.18, 0.07, and 0.03 mag, respectively. Therefore, the color spread of a sample of galaxies would, *for a given age spread*, be smaller for larger average ages. As we will show in the following section, the dE(nN)s exhibit somewhat younger stellar populations than the dE(N)s, thus providing a “natural” cause of the observed difference in CMR scatter. Similarly, this could account for the rather large scatter of the dE(bc)s in $g - i$ that is seen in Figure 1.

9. STELLAR POPULATIONS

9.1. Population synthesis models

We now attempt to use our color measurements for drawing conclusions about the actual stellar population characteristics of our galaxies. For this purpose, we construct several stellar population models, using the population synthesis code from Bruzual & Charlot (2003). Following the recommendation of the authors, we use “Padova 1994” isochrones (Bertelli et al. 1994), as well as a Chabrier initial mass function (IMF; Chabrier 2003). We use the Bruzual & Charlot high resolution files, which rely on the STELIB spectral library in the wavelength range 3200–9500 Å and on the BaSeL 3.1 spectral library outside this range (see Bruzual & Charlot 2003, and references therein). All Bruzual & Charlot models were calculated with fixed metallicity, i.e., they do not take into account chemical enrichment. When adopting a concordance cosmology ($H_0 = 71$ km s⁻¹ Mpc⁻¹, $\Omega_m = 0.27$, $\Omega_\Lambda = 0.73$), it is now 13.67 Gyr since the Big Bang (Wright 2006). We thus assume that the first stars have formed ~ 13.5 Gyr ago (also see Kashlinsky et al. 2007), which is relevant for our model with constant star formation rate (see below). All of our models are constructed for three of the seven available metallicities, namely $Z = 0.008$ ($[\text{Fe}/\text{H}] = -0.33$), $Z = 0.004$ ($[\text{Fe}/\text{H}] = -0.64$), and $Z = 0.0004$ ($[\text{Fe}/\text{H}] = -1.65$).

Firstly, we construct a commonly used model, namely a stellar population formed through a single peak of star formation that exponentially decays with time (illustrated in the top panel of Figure 9). We choose decay times of $\tau = 1$ Gyr (the *exp-1* model) and 2 Gyr (*exp-2* model). The resulting model tracks are shown in the left column of Figure 10 in various color-color diagrams. The tracks are curves of constant metallicity, and span a range of ages, from 1 to 13.5 Gyr. Here, “age” means the time since the beginning of the star formation.

Secondly, we construct a model based on the study of Davies & Phillipps (1988), who proposed a scenario for dE formation in which a dwarf irregular (dIrr) experiences several short intense bursts of star formation, during which it would appear as blue compact dwarf (BCD). These bursts would increase the initial metallicity and surface brightness of the dIrr, such that, after some time of passive evolution and fading, it would eventually appear as dE. Davies & Phillipps suggest ten bursts within a period of 1 Gyr, each one with a duration of 10 Myr. We thus construct a corresponding model (*burst* model) with 10 bursts of star formation, the tenth one occurring 0.9 Gyr after the beginning of the first one (middle panel of Figure 9). Each “burst” is a period of constant star formation rate (SFR) with a duration of 10 Myr. The corresponding model tracks are shown in the middle column of Figure 10. Here, “age” means the time since the beginning of the first star formation burst.

Thirdly, we construct a model that is intended to represent the popular scenario of dE formation through infall of a late-type galaxy into the cluster (e.g. Moore et al. 1996). The galaxy experiences a short period of enhanced star formation through gas compression and similar effects, and is then stripped of its remaining gas. This model (*const-b100* model) is defined by a constant SFR since 13.5 Gyr ago, i.e., since the formation of the first stars within our adopted cosmology (see above). Star formation is subsequently boosted by a factor of 100 during

a short period of 10 Myr, and is finally truncated (lower panel of Figure 9). The corresponding model tracks, shown in the right column of Figure 10, are thus not tracks along different formation ages, but along different truncation times. The analogue to a *young age* in the *exp* and the *burst* models therefore is a *recent truncation* of star formation in the *const-b100* model, whereas a larger age would correspond to a less recent truncation of star formation. Note that the model tracks shown for the *exp* and the *burst* models actually consist of all age points provided by Bruzual & Charlot (2003) (60 points or more), whereas the truncation times of the *const-b100* model have only been calculated by us for the points shown in the figure, which we then simply connected by lines.

The reason for plotting the model tracks in various combinations of color-color diagrams (Figure 10) is to find out which combination of colors would come closest to breaking the famous age-metallicity degeneracy (even if this cannot be achieved entirely with only optical photometry at hand). In addition, we also need to take into account that the three bands g , r , and i provide the best S/N, whereas the S/N is a few times lower in z and almost ten times lower in u . Each color-color diagram basically relates a “blue” color (on the y -axis) to a “red” color (on the x -axis).

It can be clearly seen in Figure 10 that the age-metallicity degeneracy is very strong in the cases in which the r band is used in the red color — $i - z$ therefore is the obvious choice, since it provides the reddest possible color. For the blue color, we first note that $u - r$ does a better job in breaking the degeneracy than $u - g$, since the color ranges covered by the models are larger for the former, but the errors are similar, if not smaller, in $u - r$. However, given the considerably smaller errors, $g - r$ is a useful alternative. We will therefore use both the $u - r$ vs. $i - z$ and the $g - r$ vs. $i - z$ diagram in our analysis in Section 9.2. As an aside, note that for the *burst* model, the tracks are somewhat less squeezed together in $g - r$ vs. $i - z$ than in $u - r$ vs. $i - z$.

Before we proceed towards the application of our models, we briefly comment on possible variants of our models. The main effect of weakening or amplifying the final star formation burst in the *const-b100* model is a shift towards less recent truncation times: in the case of no final burst and star formation being truncated 0.5 Gyr ago, the colors are similar to the *const-b100* model and truncation occurring 1 Gyr ago, or to a model with a three times stronger final burst and truncation occurring ~ 1.5 Gyr ago. Likewise, the dominating effect of a truncation of star formation in the *exp* models is a shift towards younger ages.

9.2. Comparison of models and data

It is generally difficult to directly compare average color values of different dE subsamples, since they are usually not sampled equally in luminosity, and thus already have different colors due to the correlation of color and magnitude. Therefore, we simply compare the color values of the linear fits to the CMR of each subsample, measured at the bright and faint “reference magnitudes”, as defined in Section 6. This is shown in Figures 11 and 12, along with the model tracks. In the left part of each figure, we use the $u - r$ vs. $i - z$ diagrams for compari-

son with the models, while the $g - r$ vs. $i - z$ diagrams are used in the right part. On each side, the respective left column shows the color values at the bright reference magnitude, while the right column shows the values at the faint reference magnitude. We also compare the colors measured within our three different apertures: the smallest symbol represents the small aperture, the largest symbol stands for the large aperture, so that gradients can be recognized. Models are shown as lines of constant metallicity in Figure 11 and as lines of constant age in Figure 12. We note again that the CMRs of the dE(bc)s and dE(di)s are only constrained by a handful of data points at fainter magnitudes. The resulting color values should thus be taken with a grain of salt, at least at the faint reference magnitude.

We first focus on the color values at the bright reference magnitude. A systematic gradient can be seen for the dE(N)s, in the sense that the stars in the inner regions of the galaxies have on average higher metallicities and possibly also somewhat younger ages. A very similar trend was also found for low-mass early-type dwarfs in the Local Group (Harbeck et al. 2001). The dE(nN)s also show color differences with radius, but the direction of the gradient is not as well-defined as for the dE(N)s: in the $u - r$ vs. $i - z$ diagrams, the colors for the small and intermediate aperture would imply an almost equal metallicity but different age, whereas in the $g - r$ vs. $i - z$ diagrams they would suggest a roughly equal age. The colors within the large aperture correspond to a lower metallicity and older age as compared to the other apertures in both the $u - r$ vs. $i - z$ and $g - r$ vs. $i - z$ diagrams. For the dE(di)s, the colors within the large aperture also seem to hint at a higher age, but no clear gradient can be seen between the apertures. Again, this might be partly due to the only moderate sample size. The dE(bc)s seem to have higher metallicities in the outskirts than in the center — here, near-infrared photometry would be desirable to guarantee that the “red color” used in the diagrams is not affected by the light of the young stars that are present in the center.

The figures illustrate that, within our simplified framework of models, the stars of the dE(nN)s are, on average, either younger⁶ than those of the dE(N)s, or of lower metallicity, or both. Unfortunately, the famous age-metallicity degeneracy prevents us from making a more definite statement, but in any case, the stellar population characteristics of dE(N)s and dE(nN)s differ. The dE(di)s appear to be on average slightly younger and/or slightly less metal-rich than the dE(N)s, a result that is more pronounced in the $g - r$ vs. $i - z$ than in the $u - r$ vs. $i - z$ diagrams. They are, however, older and/or more metal-rich than the dE(nN)s. Overall, the metallicities of the various subclasses lie at or below the track for $[\text{Fe}/\text{H}] = -0.64$ — however, care must be taken with absolute numbers, given the assumptions and simplifications on which the models are based.

At the faint reference magnitude, the differences between the subclasses are smaller, and no systematic gra-

⁶ Note that this statement does not constrain the actual star formation history. If star formation began at the same epoch in both the dE(nN)s and dE(N)s, but lasted longer in the dE(nN)s, the stars of the latter would be younger on average. The same age difference could, however, be achieved if star formation began at a later epoch, but did not last longer than in the dE(N)s.

dient within them can be seen. In the $g-r$ vs. $i-z$ diagrams the dE(nN)s still appear to be somewhat younger and/or less metal-rich than the dE(N)s, but the difference is smaller than at the bright reference magnitude, and it is even smaller in the $u-r$ vs. $i-z$ diagrams. There is still a tendency for the dE(nN)s to have lower metallicities and/or older ages in the outer regions than in the center, while for the dE(N)s, there is a slight reverse trend. However, we recall that the scatter in $i-z$ at fainter magnitudes is rather large.

10. SUMMARY AND DISCUSSION

We have analyzed the colors of 413 Virgo cluster dEs by constructing color-magnitude relations (CMRs) for different dE subclasses and different local densities, as well as by comparing them to theoretical colors from population synthesis models of Bruzual & Charlot (2003). We found significant differences between the CMRs of dE(N)s and dE(nN)s, as well as between the CMRs at low and high local projected densities. The models imply that the brighter dE(nN)s are younger than the dE(N)s and/or have lower metallicities. The dE(di)s are more similar to the dE(N)s, yet still seem to be slightly younger and/or less metal-rich on average. A significant intrinsic color scatter of the CMR is present. The color residuals about the CMR are correlated between different colors for the dE(N)s, and partly also for the dE(nN)s, such that a galaxy falling on the blue side of the CMR in one color also does so in the other color. We find no increase in the color scatter at fainter magnitudes down to $m_r \approx 17$ mag ($M_r \approx -14$ mag).

The dE(N)s are consistent with having a nearly “perfect” intrinsic correlation of colors, i.e., if the intrinsic $u-r$ color of a dE(N) lies on the red side of the respective CMR, the same is true in almost all cases for the intrinsic $i-z$ color. This is particularly interesting, since $u-r$ is more sensitive to the age of the stellar population, while $i-z$ is sensitive to metallicity. A simple, straightforward interpretation is that when the stars in a dE are on average older than the typical value at that dE’s luminosity, then they are also more metal rich, and vice versa. Assuming a direct correlation between luminosity and galaxy mass, we can speculate that the intrinsic scatter of the CMR could, for a given initial mass, reflect a spread in star formation rate or in the efficiency with which gas is turned into stars, perhaps caused by environmental effects. Neglecting other possible effects, a higher SFR at a given initial (gas) mass would lead to stronger enrichment, i.e. to a higher metallicity, than a lower SFR. The gas would be consumed more rapidly, thus reaching the end of star formation earlier than with a lower SFR, and consequently yielding older stars on average.

10.1. Subclass colors and stellar populations

While we found in Section 6 that dE(nN)s and dE(N)s follow different CMRs, we then discovered in Section 7 that the CMR depends on environmental density. Since dE(nN)s and dE(N)s populate different density regimes (Paper III), we should compare the CMR of the dE(nN)s to that of the *low-density* subsample of dE(N)s: the median density of the latter is 1.18 (in units of the logarithm of the number of galaxies per square degree), and it is 1.20 for the dE(nN)s. In contrast, the median density of

the full sample of dE(N)s is 1.37. However, the CMR of the low-density dE(N)s is still significantly different from that of the dE(nN)s in $g-r$ and $g-i$; the probability for a common distribution is $\leq 0.1\%$ for the half-light aperture. Likewise, the color difference between dE(N)s and dE(nN)s at the bright reference magnitude is 0.09 mag in $u-r$ and 0.05 mag in both $g-r$ and $g-i$, using the half-light aperture. This difference only changes by 0.01 mag in $u-r$ and $g-i$ and even less in $g-r$ when considering only the low-density dE(N)s. Thus, the colors of the (bright) dE(nN)s do differ from those of the dE(N)s even if we allow for the different sampling in density.

The same test can be done for the dE(di)s: their densities (median value 1.18) are also much more comparable to those of the low-density dE(N)s than to those of the full sample. While the color difference between the dE(di)s and the full dE(N) sample at the bright reference magnitude is only 0.02 mag in $u-r$, 0.03 mag in $g-r$, and 0.04 mag in $g-i$, the statistical comparison of their CMRs yields significant differences (Section 6). This changes when we compare the dE(di)s to only the low-density dE(N) sample. Although the colors of the dE(di)s are still slightly bluer than those of the low-density dE(N)s, none of these differences is statistically significant. Whether or not this could indicate a close relation between dE(di)s and dE(N)s despite their very different shapes will be discussed in Section 10.2.

Rakos & Schombert (2004) determined ages and metallicities for 91 dEs in the Coma and Fornax clusters, based on narrowband photometry. They derived ages above 8 Gyr for the dE(N)s, which they found to be about 5 Gyr older than the dE(nN)s. At least qualitatively, and in a relative sense, this would be consistent with our results. As for the metallicities, Rakos & Schombert found the dE(N)s to have *lower* metallicities than the dE(nN)s, conjecturing that “globular clusters and dEN galaxies are primordial and have metallicities set by external constraints such as the enrichment of their formation clouds.” This is not in agreement with our results for the brighter magnitudes: there, we find the metallicities of the dE(N)s to be either similar (in the inner part of the galaxies, see Figure 11) or higher (Figure 12) than those of the dE(nN)s. Due to the fact that the Virgo cluster is a dynamically less relaxed structure than the Coma and Fornax clusters, it would be particularly interesting to find systematic differences in the stellar content of their galaxy populations. However, it would be premature to conclude that the dE(nN)s and dE(N)s in Virgo behave inversely to those in the other clusters — the sample of Rakos & Schombert (2004) only comprises 10 dE(nN)s of the Coma cluster and 9 dE(nN)s of the Fornax cluster, and moreover, the dE(nN)s show a considerable color scatter in the metallicity-sensitive color $i-z$. Whether or not these issues can account for the differences needs to be analyzed in future work.

The question of whether our fitted CMRs would be consistent with being mainly a luminosity-metallicity relation can be qualitatively addressed by comparing the respective CMR values at the bright and faint reference magnitude in Figure 12. Overall consistency with this interpretation is present for all subclasses, but we cannot exclude the additional presence of at least some age differences with magnitude. A general problem for the interpretation of the colors also is that the color values

for some data points lie at “too large” an age, i.e., they fall above the age of the Universe for our model tracks. We thus need to emphasize again that many simplifications entered the calculation of these tracks, like the fact that the models are calculated at a fixed metallicity, or the rather simple star formation histories that we consider. All our interpretations of observed dE colors are always done within this simplified framework of stellar population models.

10.2. *The minimum number of formation scenarios*

On the basis of our observational analyses presented here and in the previous papers of this series, we now attempt to answer the question of how many different dE formation mechanisms there must be *at least* in order to explain the diversity of dE subclasses. To start with, how confident can we be that the (flat) dE(di)s do not belong to the same intrinsic (sub-)class as the (round) dE(N)s? The distribution of intrinsic shapes of the brighter dE(N)s, as deduced in Paper III, is rather broad and includes a significant number of flat objects, even down to axial ratios of 0.3. Most of the range of intrinsic axial ratios of the dE(di)s is thus covered by the range of values of the dE(N)s. Moreover, 73% of the dE(di)s are nucleated. While their colors are somewhat different from the full sample of dE(N)s, the difference is not anymore significant when compared only to the low-density dE(N)s, which have the same median density as the dE(di)s (Section 10.1).

If disk substructure, like spiral arms or bars, could only occur in the flattest dEs, due to, e.g., the kinematical configuration of these objects, we would have automatically selected only intrinsically flat galaxies in our search for disk features (Paper I), and would obviously have found their flattening distribution to be consistent with disk galaxies. The fact that these show no central clustering could then be explained, for example, by the much stronger tidal heating that a galaxy experiences in denser regions of the cluster, leading to an earlier destruction of disk features (cf. Mastroiello et al. 2005). Similarly, if dE(N)s and dE(di)s originated from a morphological transformation of infalling late-type spirals through galaxy harassment (Moore et al. 1996), one could imagine that the amount of transformation depended on how close the encounters with massive galaxies were that led to it — and the probability for close(r) encounters is obviously higher in the cluster center, leading to rounder objects without disk features.

Why, then, are there almost no fainter dE(di)s? While we concluded in Paper I that we most likely missed a significant amount of dE(di)s at fainter magnitudes due to our detection limits, we also argued that the true number fraction *does* decrease when going to fainter objects. As a possible explanation, we can speculate that disk substructure might be more likely to occur in more massive galaxies, possibly connected to the presence of a certain amount of rotational velocity. These qualitative considerations demonstrate that dE(di)s and dE(N)s could, in principle, have formed through the same formation process, keeping our counter of necessary dE formation mechanisms at 1 for the moment.

Could the dE(nN)s be also related to the dE(N)s and be formed by the same process? At least for the bright subsamples, the colors of dE(nN)s and dE(N)s differ sig-

nificantly, indicating younger average stellar ages of the dE(nN)s, or lower metallicities, or both (Section 9). This still holds true even when the different density distributions of dE(nN)s and dE(N)s are accounted for (Section 10.1). One might thus conjecture that the dE(nN)s simply formed more recently. The significantly flatter shapes of the bright dE(nN)s could then possibly be explained in the sense that they still need to experience several (further) encounters with massive galaxies, leading to further morphological transformation. One would, though, need to invoke another assumption, namely that the faint dE(nN)s, which are already significantly rounder than the bright dE(nN)s, were much more affected by the first tidal encounters, while the bright dE(nN)s were able to partly preserve their initial shape⁷ — this could possibly be explained by the difference in mass.

Another requirement of this scenario would be that the distribution of dE(nN)s within the cluster, which is not centrally concentrated at all (Paper III), would need to shift towards significantly larger local densities within the next few Gigayears, in order to be similar to the distribution of today’s dE(N)s. However, Conselice et al. (2001) derived a two-body relaxation time for the Virgo dEs of much more than a Hubble time. Even violent relaxation, which probably only applies for the case of infalling or merging groups, would take at least a few cluster crossing times t_{cr} , with $t_{\text{cr}} \approx 1.7$ Gyr for Virgo (Boselli & Gavazzi 2006). It thus seems difficult to reconcile these numbers with the required dynamical process.

A further, obvious point is that nuclei would need to form soon in the dE(nN)s. Perhaps nuclei are currently being formed in the centers of the dE(bc)s where we are witnessing ongoing star formation (Paper II). Such a scenario would lead to nuclei whose stars were clearly younger than the vast majority of their host galaxies’ stars. This would, however, be hardly consistent with the results of Côté et al. (2006), who found “old to intermediate-age populations” of dE nuclei, and of Lotz et al. (2004a), who measured similar colors of nuclei and dE globular clusters. An alternative would be that most nuclei form through coalescence of globular clusters (e.g. Oh & Lin 2000). Yet in neither case do we find an explanation for why the ratio of nucleated and non-nucleated dEs should increase strongly with luminosity (Sandage et al. 1985) if the latter were the immediate progenitors of the former.

Taken together, our observational results do not allow to explain dE formation with less than two different processes. We thus conclude by repeating the statement of van Zee et al. (2004), “we caution against single-channel evolutionary scenarios.” Early-type dwarfs are not a homogeneous class of objects, and we strongly recommend to separately analyze the properties of dEs belonging to different subclasses in any future study of dEs.

We wish to express our gratitude to Mischa Vodička for performing a preliminary photometric analysis of our dE sample, which helped us in optimizing our methods

⁷ However, note that the bright dE(nN)s might not even have experienced any tidal encounters yet, but could have been born as thick, puffy systems (Kaufmann et al. 2007).

for image treatment and galaxy photometry. We thank Niranjana Sambhus for useful comments on statistical tests, and the referee for valuable suggestions. We gratefully acknowledge support by the Swiss National Science Foundation through grants number 200020-105260 and 200020-105535. T.L. is supported within the framework of the Excellence Initiative by the German Research Foundation (DFG) through the Heidelberg Graduate School of Fundamental Physics (grant number GSC 129/1). T.L. would like to thank Martin Altmann for useful SM macros.

This study would not have been possible without the wealth of publicly available data from the SDSS. Funding for the SDSS has been provided by the Alfred P. Sloan Foundation, the Participating Institutions, the National Science Foundation, the U.S. Department of Energy, the National Aeronautics and Space Administration, the Japanese Monbukagakusho, the Max Planck Society, and the Higher Education Funding Council for England. The SDSS Web Site is <http://www.sdss.org/>.

The SDSS is managed by the Astrophysical Research Consortium for the Participating Institutions. The Par-

ticipating Institutions are the American Museum of Natural History, Astrophysical Institute Potsdam, University of Basel, Cambridge University, Case Western Reserve University, University of Chicago, Drexel University, Fermilab, the Institute for Advanced Study, the Japan Participation Group, Johns Hopkins University, the Joint Institute for Nuclear Astrophysics, the Kavli Institute for Particle Astrophysics and Cosmology, the Korean Scientist Group, the Chinese Academy of Sciences (LAMOST), Los Alamos National Laboratory, the Max-Planck-Institute for Astronomy (MPIA), the Max-Planck-Institute for Astrophysics (MPA), New Mexico State University, Ohio State University, University of Pittsburgh, University of Portsmouth, Princeton University, the United States Naval Observatory, and the University of Washington.

This research has made use of NASA’s Astrophysics Data System Bibliographic Services, and of the NASA/IPAC Extragalactic Database (NED) which is operated by the Jet Propulsion Laboratory, California Institute of Technology, under contract with the National Aeronautics and Space Administration.

APPENDIX

A. THE PETROSIAN UNCERTAINTY

The uncertainty in the determination of the Petrosian SMA is difficult to estimate, and even more so the subsequent uncertainty in the total r band flux and the corresponding half-light SMA. Apart from proper masking of neighbouring or blended objects – which we assume to have been done sufficiently accurately – the determination of the Petrosian SMA is strongly affected by a possible over- or underestimation of the sky level. Should the sky level be overestimated, as is the case in the measurements of the SDSS photometric pipeline (see Lisker et al. 2005), the Petrosian SMA will be underestimated, and vice versa. Thus, in the case of a sky level overestimation, the total galaxy flux will be underestimated due to both the sky flux oversubtraction *and* the lower-than-actual Petrosian SMA within which the flux is measured. We thus assume the “Petrosian uncertainty” to be of the same order as the sky level uncertainty (see Section 4), which we therefore simply count twice in our calculation of total errors.

The Petrosian uncertainty is not directly relevant for the calculation of a *color* value of a given galaxy from the flux values of two bands, since the aperture used is the same for both bands, independent of whether its size was under- or overestimated. However, it is relevant for comparing the color values of two different galaxies, since for one of them, the half-light SMA might have been underestimated, but overestimated for the other. In order to obtain a conservative error estimate for the colors, we therefore decided to take into account the Petrosian uncertainty in the same way as for the r band total flux, even if this might be somewhat too pessimistic.

B. STATISTICAL COMPARISON OF TWO COLOR-MAGNITUDE RELATIONS

Here we elaborate in more detail on our method of statistically comparing two given color-magnitude relations (Section 5.2). Obviously, one would consider two CMRs to be different if either their slopes, their zeropoints, or both were significantly different from each other. Unfortunately, our method of linear fitting described in Section 5.1 does not yield errors on these parameters — but even with a method that would yield formal errors, like least-squares fitting, it is often the case that these errors are not realistic (Press et al. 2002). The alternative to comparing the fitted lines would be to compare the two underlying datasets directly. However, here we face the problem that these might have different average magnitudes, like, e.g., the $dE(N)$ s and the $dE(nN)$ s. For example, for two given datasets that follow exactly the same CMR but probe different magnitude regimes, a two-dimensional K-S test would yield a probability of zero that the datasets have the same underlying distribution, simply because they are significantly different in the magnitude-dimension. This is clearly not the sort of test we want to perform.

Given the above considerations, we decided on an approach that combines a comparison of both the data points and the fitted lines of two datasets A and B. First, we compute the color residuals of the data points A and the data points B about the CMR A. This gives us two distributions of a single parameter, namely the residual about the CMR A, independent of magnitude. We can now compare these two distributions with each other through a (one-dimensional) K-S test, which compares the cumulative distributions, and through a Student’s t-test for unequal variances, which compares the means of the distributions. We then compute analogously the residuals of the data points A and B about the CMR B. For the K-S test, we take the average of both values of the K-S statistic D (which is the maximum difference between two cumulative distributions, see Press et al. 2002), and compute our final probability from it. For the t-test, we simply use the larger of the two probabilities as our final probability.

The K-S test has the advantage that it is sensitive to different distributions around the CMR, even if the mean of both was zero, e.g. if both CMRs had different slopes but crossed each other at the middle data point. The Student’s

t-test for unequal variances has the advantage of taking into account the scatter of each dataset around the mean, which implicitly includes the measurement errors. Note that the goodness of the linear fit is only taken into account implicitly to a small extent: if one of the two linear relations was a rather bad fit or was based on a small sample with large scatter, this would partially be counterbalanced by the inverse comparison with the other CMR. If, however, both linear fits were rather weakly defined, the resulting probabilities might not be too useful.

C. THE SCATTER OF THE COLOR-MAGNITUDE RELATION

In order to obtain a rough estimate of the *true* scatter of the CMR (i.e., that is not caused by measurement errors), we can compare the observed scatter with our measurement errors. The respective values are given in Table 1: the column “rms” gives the root mean square of the color residuals about the linear fit to the CMR, while the column “E-rms” gives the root mean square of the errors. If the observed scatter was solely due to measurement errors, these two values should be similar, at least for the larger (i.e., statistically robust) dE subsamples. The ratio of the two values, which is given in the last column of the table, is thus an indirect measure of the true scatter; we refer to it as the “rms-ratio”. The *true* scatter can be a combination of an *intrinsic* color scatter and a distance spread; we shall consider the latter at the end of this section.

We first note that for most CMRs, the rms-ratio increases with aperture size. As for a possible intrinsic color scatter, it can hardly be deduced whether, and how strongly, it increases from the inner to the outer parts of the dEs. As for our measurement errors, we know that they consist of one part that remains constant with aperture size, namely the error on the photometric calibration zeropoint (“calibration uncertainty”, see Section 4), and another part that increases with aperture size, namely the S/N uncertainty and the sky level uncertainty. It thus appears likely that an overestimation of the calibration uncertainty causes, at least partly, the observed increase in the rms-ratio with aperture size: due to this uncertainty, the measurement errors do not approach zero with increasing S/N, but instead reach a finite value. If this value – which is provided directly by the SDSS for each color – would be overestimated, the rms-ratio would fall below a value of 1 for high-S/N measurements, which is indeed the case for some of the small-aperture CMRs, like e.g., for the bright dE(N)s in $i-z$. Again, we are not able to tell how much of the increase in the rms-ratio is an intrinsic effect, but the above considerations suggest that the photometric calibration might be at least somewhat better than estimated.

We now attempt to derive an estimate for how large the true scatter is with respect to our measurement uncertainties, i.e., which of the two dominates the observed scatter. Given the above findings, we focus only on the rms-ratios for the large-aperture CMRs, in order to not underestimate the true scatter. When we consider only the larger dE subsamples, i.e., the bright and faint dE(N)s, the faint dE(nN)s, and the full samples of dE(N)s, dE(nN)s, and all dEs, we find that the rms-ratio always lies between 1.3 and 2. With the simplifying assumption that the rms of the true scatter and the rms of the measurement uncertainties add quadratically to yield the observed rms, these values would imply that the rms of the true scatter lies between 0.8 and 1.7 of that of the measurement uncertainties.

We now attempt to estimate how the fraction of galaxies within the different quadrants (Figure 7) would be distributed given a perfect correlation plus measurement errors. With “perfect correlation”, we mean that each galaxy falling on one side of the CMR in one color falls on the same side of the CMR in the other color. We only care about the *direction* of the color offset, i.e., the sign of the residual, not about its absolute value. In the following, we describe for the correlation of $u-r$ vs. $g-i$ how we simulate a CMR scatter. This simulation is done in the same way for the other color pairs.

In order to keep our approach simple, yet still instructive, we refrain from choosing a certain analytic model distribution for the true scatter of $u-r$ and $g-i$. Instead, we adopt the *observed* distribution of color values as one possible example for a true distribution. To guarantee that a given galaxy falls on the same side of the CMR for both colors, simulating a perfect correlation, we assign to the $g-i$ residual of each galaxy the sign of its corresponding $u-r$ residual (but keep its absolute value). This represents our simulated distribution of true⁸ residuals. For simulating the distribution of measurement uncertainties, we use again the observed distribution of color residuals, but redistribute these values randomly among our galaxies, and assign them random signs. We then add these values to the simulated true residuals, thereby yielding simulated observed residuals. Note that in this case, the rms of the true scatter and of the measurement uncertainties are obviously equal, since we used the same absolute values. This can be altered by multiplying the simulated true residuals with a certain factor.

The simulation was performed for the full dE sample (excluding dE(bc)s), and was repeated 1000 times for all three independent color pairs (i.e., $u-r$ vs. $g-i$, $u-r$ vs. $i-z$, and $g-r$ vs. $i-z$). We chose the rms value of the true scatter to be 0.8 and 1.7 times as large as the rms of the measurement uncertainties in order to test our values deduced above. For simplicity, we term these two cases the “0.8-case” and “1.7-case”, respectively. For $u-r$ vs. $g-i$, the resulting median fraction of galaxies within the upper right and lower left quadrants is 63% for the 0.8-case, and 72% for the 1.7-case. For both $u-r$ vs. $i-z$ and $g-r$ vs. $i-z$, the corresponding values are 62% and 72%. Our observed value for $u-r$ vs. $g-i$ (70%) lies between the two simulated cases and closer to the 1.7-case. For $u-r$ vs. $i-z$, the observed value is 60%, and for $g-r$ vs. $i-z$, it is 59% — both values are only slightly below the simulated 0.8-case. These results confirm that our galaxy colors can well be explained by a true scatter within the range deduced above, and that the dEs, or at least the dE(N)s, are consistent with exhibiting a strong correlation of color residuals between

⁸ Our word choice here (“*simulated* distribution of *true* residuals”) might not be ideal, but we want to avoid speaking of an “intrinsic distribution”, since the true scatter can be a combination of an intrinsic color scatter and a distance spread. With “true”, we only mean that it is not caused by measurement uncertainties.

different colors.

We now need to investigate whether part of the scatter of the CMR could be caused by a spread in distance, which would lead to a certain scatter in magnitude, and would thus contribute to the scatter of the CMR. We concentrate on the CMR of the $dE(N)$ s in $g - i$ for the large aperture. Here, the rms of our measurement errors is 0.034 mag (Table 1). Assuming the 0.8-case, the true rms scatter would be 0.027 mag. The slope of the CMR is -0.044 (Table 1). Consequently, a scatter of ± 0.027 mag around the CMR would mean a scatter of ± 0.61 mag in the distance modulus, or ${}_{-3.88}^{+5.14}$ Mpc at our adopted Virgo cluster distance of 15.85 Mpc ($m - M = 31.0$ mag). Such a huge (rms!) scatter is at variance with the observations — Jerjen et al. (2004) deduced a true dispersion in distance modulus of ± 0.177 mag, corresponding to ${}_{-1.24}^{+1.35}$ Mpc (when using our distance modulus). When we adopt this observed value as rms distance scatter, the resulting color scatter for the CMR in question is ± 0.008 mag. While this is rather small, it is nevertheless almost one third of the inferred true scatter in the 0.8-case (see above). However, the rms scatter from different uncertainties does most likely not add linearly — if the “distance uncertainty” was added *quadratically* to the intrinsic color scatter, it would have a very small effect only. In any case, while a small but finite distance scatter is naturally unavoidable, we conclude that a significant *intrinsic* color scatter must be present for our galaxies, with a strong correlation between the different colors.

REFERENCES

- Adelman-McCarthy, J. K., et al. 2007, *ApJS*, 172, 634
 Baum, W. A. 1959, *PASP*, 71, 106
 Bernardi, M., Nichol, R. C., Sheth, R. K., Miller, C. J., & Brinkmann, J. 2006, *AJ*, 131, 1288
 Bernardi, M., et al. 2003, *AJ*, 125, 1882
 Bertelli, G., Bressan, A., Chiosi, C., Fagotto, F., & Nasi, E. 1994, *A&AS*, 106, 275
 Binggeli, B. & Cameron, L. M. 1991, *A&A*, 252, 27
 Binggeli, B. & Popescu, C. C. 1995, *A&A*, 298, 63
 Binggeli, B., Popescu, C. C., & Tammann, G. A. 1993, *A&AS*, 98, 275
 Binggeli, B., Sandage, A., & Tammann, G. A. 1985, *AJ*, 90, 1681
 Binggeli, B., Tammann, G. A., & Sandage, A. 1987, *AJ*, 94, 251
 Boselli, A. & Gavazzi, G. 2006, *PASP*, 118, 517
 Bothun, G. D., Mould, J. R., Caldwell, N., & MacGillivray, H. T. 1986, *AJ*, 92, 1007
 Bower, R. G., Lucey, J. R., & Ellis, R. S. 1992, *MNRAS*, 254, 601
 Bruzual, G. & Charlot, S. 2003, *MNRAS*, 344, 1000
 Caldwell, N. 1983, *AJ*, 88, 804
 Chabrier, G. 2003, *PASP*, 115, 763
 Chang, R., Gallazzi, A., Kauffmann, G., Charlot, S., Ivezić, Ž., Brinchmann, J., & Heckman, T. M. 2006, *MNRAS*, 366, 717
 Conselice, C. J., Gallagher, III, J. S., & Wyse, R. F. G. 2001, *ApJ*, 559, 791
 —. 2002, *AJ*, 123, 2246
 —. 2003, *AJ*, 125, 66
 Côté, P., et al. 2006, *ApJS*, 165, 57
 Davies, J. I. & Phillipps, S. 1988, *MNRAS*, 233, 553
 De Rijcke, S., Michielsen, D., Dejonghe, H., Zeilinger, W. W., & Hau, G. K. T. 2005, *A&A*, 438, 491
 de Vaucouleurs, G. 1961, *ApJS*, 5, 233
 Dellenbusch, K. E., Gallagher, III, J. S., & Knezek, P. M. 2007, *ApJ*, 655, L29
 Dressler, A. 1980, *ApJ*, 236, 351
 Faber, S. M. 1973, *ApJ*, 179, 731
 Faber, S. M. & Jackson, R. E. 1976, *ApJ*, 204, 668
 Gavazzi, G., Boselli, A., Scodreggio, M., Pierini, D., & Belsole, E. 1999, *MNRAS*, 304, 595
 Graham, J. A., et al. 1999, *ApJ*, 516, 626
 Grebel, E. K., Gallagher, J. S., & Harbeck, D. 2003, *AJ*, 125, 1926
 Gunn, J. E., et al. 1998, *AJ*, 116, 3040
 Harbeck, D., Grebel, E. K., Holtzman, J., Guhathakurta, P., Brandner, W., Geisler, D., Sarajedini, A., Dolphin, A., Hurley-Keller, D., & Mateo, M. 2001, *AJ*, 122, 3092
 Jerjen, H., Binggeli, B., & Barazza, F. D. 2004, *AJ*, 127, 771
 Kashlinsky, A., Arendt, R. G., Mather, J., & Moseley, S. H. 2007, *ApJ*, 654, L1
 Kaufmann, T., Wheeler, C., & Bullock, J. S. 2007, *MNRAS*, submitted, arXiv:0706.0210
 Kodama, T. & Arimoto, N. 1997, *A&A*, 320, 41
 Lisker, T., Glatt, K., Westera, P., & Grebel, E. K. 2006b, *AJ*, 132, 2432, *Paper II*
 Lisker, T., Grebel, E. K., & Binggeli, B. 2005, in *IAU Colloq. 198: Near-field cosmology with dwarf elliptical galaxies*, ed. H. Jerjen & B. Binggeli (Cambridge: CUP), 311
 Lisker, T., Grebel, E. K., & Binggeli, B. 2006a, *AJ*, 132, 497, *Paper I*
 Lisker, T., Grebel, E. K., Binggeli, B., & Glatt, K. 2007, *ApJ*, 660, 1186, *Paper III*
 Lotz, J. M., Miller, B. W., & Ferguson, H. C. 2004a, *ApJ*, 613, 262
 Lotz, J. M., Primack, J., & Madau, P. 2004b, *AJ*, 128, 163
 Mastropietro, C., Moore, B., Mayer, L., Debattista, V. P., Piffaretti, R., & Stadel, J. 2005, *MNRAS*, 364, 607
 Matković, A. & Guzmán, R. 2005, *MNRAS*, 362, 289
 Moore, B., Katz, N., Lake, G., Dressler, A., & Oemler, A. 1996, *Nature*, 379, 613
 Neilsen, Jr., E. H. & Tsvetanov, Z. I. 2000, *ApJ*, 536, 255
 Oh, K. S. & Lin, D. N. C. 2000, *ApJ*, 543, 620
 Oke, J. B. & Gunn, J. E. 1983, *ApJ*, 266, 713
 Petrosian, V. 1976, *ApJ*, 209, L1
 Pier, J. R., Munn, J. A., Hindsley, R. B., Hennessy, G. S., Kent, S. M., Lupton, R. H., & Ivezić, Ž. 2003, *AJ*, 125, 1559
 Poggianti, B. M., et al. 2001, *ApJ*, 562, 689
 Press, W. H., Teukolsky, S. A., Vetterling, W., & Flannery, B. P. 2002, *Numerical recipes in C++ : the art of scientific computing* (2nd ed.; Cambridge: CUP)
 Rakos, K. & Schombert, J. 2004, *AJ*, 127, 1502
 Sabatini, S., Davies, J., van Driel, W., Baes, M., Roberts, S., Smith, R., Linder, S., & O’Neil, K. 2005, *MNRAS*, 357, 819
 Richer, M., McCall, M. L., & Stasinska, G. 1998, *A&A*, 340, 67
 Sandage, A., Binggeli, B., & Tammann, G. A. 1985, *AJ*, 90, 1759
 Sandage, A. & Visvanathan, N. 1978a, *ApJ*, 225, 742
 —. 1978b, *ApJ*, 223, 707
 Schlegel, D. J., Finkbeiner, D. P., & Davis, M. 1998, *ApJ*, 500, 525
 Secker, J., Harris, W. E., & Plummer, J. D. 1997, *PASP*, 109, 1377
 Stoughton, C., et al. 2002, *AJ*, 123, 485
 Thuan, T. X. 1985, *ApJ*, 299, 881
 Vaduvescu, O. & McCall, M. L. 2005, in *IAU Colloq. 198: Near-field cosmology with dwarf elliptical galaxies*, ed. H. Jerjen & B. Binggeli (Cambridge: CUP), 265
 van den Bergh, S. 1996, *PASP*, 108, 1091
 van Zee, L., Skillman, E. D., & Haynes, M. P. 2004, *AJ*, 128, 121
 West, M. J. & Blakeslee, J. P. 2000, *ApJ*, 543, L27
 Wright, E. L. 2006, *PASP*, 118, 1711

TABLE 1
 COLOR-MAGNITUDE RELATION PARAMETERS.

Type	Color	Aperture	Zeropoint (mag)	Slope	rms (mag)	E-rms (mag)	Ratio
dE(N)	<i>u-r</i>	small	3.451	-0.0986	0.146	0.139	1.046
dE(N)	<i>u-r</i>	interm.	3.168	-0.0810	0.127	0.102	1.236
dE(N)	<i>u-r</i>	large	3.299	-0.0922	0.177	0.113	1.567
dE(N)	<i>g-r</i>	small	1.008	-0.0258	0.040	0.035	1.150
dE(N)	<i>g-r</i>	interm.	0.996	-0.0253	0.033	0.032	1.017
dE(N)	<i>g-r</i>	large	0.931	-0.0212	0.045	0.034	1.341
dE(N)	<i>g-i</i>	small	1.593	-0.0450	0.050	0.035	1.429
dE(N)	<i>g-i</i>	interm.	1.549	-0.0421	0.045	0.033	1.395
dE(N)	<i>g-i</i>	large	1.581	-0.0441	0.062	0.034	1.797
dE(N)	<i>i-z</i>	small	0.516	-0.0246	0.066	0.067	0.990
dE(N)	<i>i-z</i>	interm.	0.437	-0.0200	0.066	0.056	1.168
dE(N)	<i>i-z</i>	large	0.262	-0.0086	0.103	0.060	1.706
dE(nN)	<i>u-r</i>	small	2.558	-0.0470	0.225	0.224	1.004
dE(nN)	<i>u-r</i>	interm.	2.789	-0.0616	0.255	0.165	1.548
dE(nN)	<i>u-r</i>	large	2.896	-0.0731	0.317	0.193	1.641
dE(nN)	<i>g-r</i>	small	0.778	-0.0134	0.055	0.044	1.253
dE(nN)	<i>g-r</i>	interm.	0.711	-0.0095	0.056	0.038	1.488
dE(nN)	<i>g-r</i>	large	0.747	-0.0117	0.068	0.042	1.642
dE(nN)	<i>g-i</i>	small	1.230	-0.0246	0.070	0.044	1.565
dE(nN)	<i>g-i</i>	interm.	1.268	-0.0265	0.067	0.038	1.741
dE(nN)	<i>g-i</i>	large	1.305	-0.0285	0.074	0.042	1.764
dE(nN)	<i>i-z</i>	small	0.276	-0.0093	0.104	0.096	1.080
dE(nN)	<i>i-z</i>	interm.	0.194	-0.0046	0.106	0.075	1.424
dE(nN)	<i>i-z</i>	large	0.098	0.0003	0.159	0.095	1.665
dE(di)	<i>u-r</i>	small	3.469	-0.1047	0.150	0.062	2.433
dE(di)	<i>u-r</i>	interm.	2.924	-0.0660	0.119	0.056	2.138
dE(di)	<i>u-r</i>	large	2.695	-0.0501	0.145	0.059	2.440
dE(di)	<i>g-r</i>	small	0.970	-0.0252	0.035	0.030	1.185
dE(di)	<i>g-r</i>	interm.	0.981	-0.0261	0.034	0.030	1.151
dE(di)	<i>g-r</i>	large	0.997	-0.0270	0.030	0.030	1.013
dE(di)	<i>g-i</i>	small	1.609	-0.0493	0.056	0.030	1.876
dE(di)	<i>g-i</i>	interm.	1.603	-0.0481	0.052	0.030	1.770
dE(di)	<i>g-i</i>	large	1.727	-0.0566	0.055	0.030	1.826
dE(di)	<i>i-z</i>	small	0.503	-0.0241	0.024	0.040	0.585
dE(di)	<i>i-z</i>	interm.	0.397	-0.0167	0.033	0.042	0.784
dE(di)	<i>i-z</i>	large	0.539	-0.0275	0.059	0.044	1.358
dE(bc)	<i>u-r</i>	small	4.911	-0.2251	0.184	0.049	3.771
dE(bc)	<i>u-r</i>	interm.	3.463	-0.1169	0.135	0.057	2.388
dE(bc)	<i>u-r</i>	large	4.445	-0.1879	0.127	0.050	2.533
dE(bc)	<i>g-r</i>	small	0.789	-0.0198	0.078	0.030	2.576
dE(bc)	<i>g-r</i>	interm.	0.727	-0.0127	0.066	0.030	2.198
dE(bc)	<i>g-r</i>	large	0.607	-0.0035	0.058	0.030	1.930
dE(bc)	<i>g-i</i>	small	1.175	-0.0295	0.116	0.030	3.811
dE(bc)	<i>g-i</i>	interm.	1.230	-0.0296	0.094	0.030	3.121
dE(bc)	<i>g-i</i>	large	1.270	-0.0304	0.078	0.030	2.556
dE(bc)	<i>i-z</i>	small	0.382	-0.0180	0.030	0.045	0.670
dE(bc)	<i>i-z</i>	interm.	0.380	-0.0177	0.019	0.039	0.482
dE(bc)	<i>i-z</i>	large	0.028	0.0081	0.033	0.044	0.750
dE	<i>u-r</i>	small	3.213	-0.0848	0.179	0.172	1.042
dE	<i>u-r</i>	interm.	3.176	-0.0830	0.186	0.128	1.459
dE	<i>u-r</i>	large	3.425	-0.1023	0.238	0.145	1.646
dE	<i>g-r</i>	small	0.966	-0.0240	0.049	0.038	1.283
dE	<i>g-r</i>	interm.	0.957	-0.0233	0.047	0.034	1.362
dE	<i>g-r</i>	large	0.946	-0.0228	0.053	0.036	1.461
dE	<i>g-i</i>	small	1.521	-0.0413	0.062	0.039	1.611
dE	<i>g-i</i>	interm.	1.492	-0.0391	0.058	0.035	1.684
dE	<i>g-i</i>	large	1.539	-0.0420	0.069	0.037	1.858
dE	<i>i-z</i>	small	0.448	-0.0204	0.072	0.076	0.946
dE	<i>i-z</i>	interm.	0.420	-0.0189	0.078	0.061	1.275
dE	<i>i-z</i>	large	0.367	-0.0161	0.119	0.074	1.597

NOTE. — “rms” is the root mean square of the color residuals about the linear fit, “E-rms” is the root mean square of the color errors, and “Ratio” is the ratio of rms and E-rms. Clipped data points are not taken into account in the calculation of the rms.

TABLE 2
 STATISTICAL COMPARISONS OF COLOR-MAGNITUDE
 RELATIONS OF EARLY-TYPE DWARF SUBCLASSES.

Type 1	Type 2	Color	Aperture	K-S test (%)	t-test (%)
dE(N)	dE(nN)	$u-r$	small	0.00	8.55
dE(N)	dE(nN)	$u-r$	interm.	0.00	6.02
dE(N)	dE(nN)	$u-r$	large	0.02	9.10
dE(N)	dE(nN)	$g-r$	small	0.00	0.00
dE(N)	dE(nN)	$g-r$	interm.	0.00	0.00
dE(N)	dE(nN)	$g-r$	large	0.00	0.04
dE(N)	dE(nN)	$g-i$	small	0.00	0.01
dE(N)	dE(nN)	$g-i$	interm.	0.00	0.00
dE(N)	dE(nN)	$g-i$	large	0.00	0.53
dE(N)	dE(nN)	$i-z$	small	15.29	68.98
dE(N)	dE(nN)	$i-z$	interm.	16.48	68.92
dE(N)	dE(nN)	$i-z$	large	15.89	29.76
dE(N)	dE(di)	$u-r$	small	0.33	1.69
dE(N)	dE(di)	$u-r$	interm.	14.86	27.66
dE(N)	dE(di)	$u-r$	large	15.43	80.99
dE(N)	dE(di)	$g-r$	small	1.17	2.28
dE(N)	dE(di)	$g-r$	interm.	0.40	1.00
dE(N)	dE(di)	$g-r$	large	3.50	11.25
dE(N)	dE(di)	$g-i$	small	0.05	0.38
dE(N)	dE(di)	$g-i$	interm.	0.03	0.92
dE(N)	dE(di)	$g-i$	large	0.74	1.60
dE(N)	dE(di)	$i-z$	small	3.89	59.39
dE(N)	dE(di)	$i-z$	interm.	0.66	16.25
dE(N)	dE(di)	$i-z$	large	1.07	48.83
dE(nN)	dE(di)	$u-r$	small	1.99	25.19
dE(nN)	dE(di)	$u-r$	interm.	2.80	37.77
dE(nN)	dE(di)	$u-r$	large	0.07	50.74
dE(nN)	dE(di)	$g-r$	small	8.60	37.56
dE(nN)	dE(di)	$g-r$	interm.	2.90	67.77
dE(nN)	dE(di)	$g-r$	large	4.59	87.08
dE(nN)	dE(di)	$g-i$	small	11.43	39.27
dE(nN)	dE(di)	$g-i$	interm.	11.52	53.16
dE(nN)	dE(di)	$g-i$	large	3.04	10.28
dE(nN)	dE(di)	$i-z$	small	1.16	40.18
dE(nN)	dE(di)	$i-z$	interm.	0.02	8.62
dE(nN)	dE(di)	$i-z$	large	0.11	41.91

NOTE. — The CMRs of a pair of dE subclasses (1st and 2nd column) are compared for a given color (3rd column) and aperture (4th column). Probabilities for a common underlying distribution are derived from a K-S test (5th column) and a Student's t-test for unequal variances (6th column); see text for details. The corresponding CMRs for the intermediate aperture are shown in Figure 1.

TABLE 3
 COLOR COMPARISON OF EARLY-TYPE DWARF SUBCLASSES.

Color	Aperture	dE(N) (mag)	dE(nN) (mag)	dE(di) (mag)	dE(bc) (mag)	dE (mag)	dE(N) _{bri.} (mag)	dE(nN) _{bri.} (mag)
Color values at the bright reference magnitude								
<i>u-r</i>	small	1.995	1.863	1.922	1.585	1.960	1.999	1.864
<i>u-r</i>	interm.	1.971	1.879	1.950	1.736	1.950	1.980	1.832
<i>u-r</i>	large	1.938	1.817	1.956	1.669	1.914	1.937	1.802
<i>g-r</i>	small	0.627	0.580	0.598	0.497	0.611	0.627	0.583
<i>g-r</i>	interm.	0.622	0.571	0.596	0.540	0.613	0.623	0.582
<i>g-r</i>	large	0.618	0.574	0.599	0.556	0.608	0.620	0.578
<i>g-i</i>	small	0.929	0.867	0.881	0.739	0.911	0.925	0.865
<i>g-i</i>	interm.	0.928	0.876	0.892	0.793	0.914	0.929	0.878
<i>g-i</i>	large	0.930	0.884	0.891	0.820	0.918	0.928	0.883
<i>i-z</i>	small	0.152	0.138	0.146	0.117	0.148	0.154	0.135
<i>i-z</i>	interm.	0.142	0.127	0.150	0.119	0.141	0.145	0.128
<i>i-z</i>	large	0.135	0.103	0.132	0.148	0.129	0.133	0.105
Color values at the faint reference magnitude								
<i>u-r</i>	small	1.823	1.781	1.740	1.193	1.812
<i>u-r</i>	interm.	1.830	1.772	1.835	1.532	1.806
<i>u-r</i>	large	1.777	1.690	1.868	1.341	1.736
<i>g-r</i>	small	0.582	0.557	0.554	0.463	0.569
<i>g-r</i>	interm.	0.578	0.555	0.551	0.518	0.573
<i>g-r</i>	large	0.581	0.554	0.552	0.550	0.569
<i>g-i</i>	small	0.850	0.824	0.795	0.688	0.839
<i>g-i</i>	interm.	0.855	0.830	0.808	0.741	0.846
<i>g-i</i>	large	0.853	0.835	0.792	0.767	0.845
<i>i-z</i>	small	0.109	0.121	0.104	0.086	0.112
<i>i-z</i>	interm.	0.107	0.119	0.121	0.088	0.108
<i>i-z</i>	large	0.120	0.103	0.084	0.162	0.101

NOTE. — Color values of the CMRs at the bright reference magnitude, $m_{r,bri.} = 14.77$ mag, and the faint reference magnitude, $m_{r,fai.} = 16.51$ mag (see text), for the three different apertures (2nd column). The two rightmost columns refer to the respective bright subsample of dE(N)s and dE(nN)s.

TABLE 4
 STATISTICAL COMPARISONS OF
 COLOR-MAGNITUDE RELATIONS FOR DIFFERENT
 DENSITIES.

Type	Color	Aperture	K-S test (%)	t-test (%)
dE(N)	$u-r$	small	7.85	4.02
dE(N)	$u-r$	interm.	1.95	0.56
dE(N)	$u-r$	large	32.11	3.87
dE(N)	$g-r$	small	93.16	24.89
dE(N)	$g-r$	interm.	6.43	3.23
dE(N)	$g-r$	large	24.55	3.14
dE(N)	$g-i$	small	8.22	2.97
dE(N)	$g-i$	interm.	1.84	2.18
dE(N)	$g-i$	large	4.83	1.09
dE(N)	$i-z$	small	5.58	44.52
dE(N)	$i-z$	interm.	65.68	86.18
dE(N)	$i-z$	large	74.50	72.22
dE(nN)	$u-r$	small	23.48	35.72
dE(nN)	$u-r$	interm.	15.43	51.11
dE(nN)	$u-r$	large	31.48	29.56
dE(nN)	$g-r$	small	47.96	19.16
dE(nN)	$g-r$	interm.	68.69	41.28
dE(nN)	$g-r$	large	35.95	52.74
dE(nN)	$g-i$	small	6.70	2.13
dE(nN)	$g-i$	interm.	10.24	4.26
dE(nN)	$g-i$	large	18.33	6.35
dE(nN)	$i-z$	small	26.07	63.19
dE(nN)	$i-z$	interm.	61.61	70.99
dE(nN)	$i-z$	large	47.96	73.07
dE	$u-r$	small	0.46	0.66
dE	$u-r$	interm.	3.01	1.65
dE	$u-r$	large	0.67	0.93
dE	$g-r$	small	0.92	0.01
dE	$g-r$	interm.	0.10	0.00
dE	$g-r$	large	0.23	0.00
dE	$g-i$	small	0.01	0.00
dE	$g-i$	interm.	0.00	0.00
dE	$g-i$	large	0.02	0.00
dE	$i-z$	small	13.24	21.72
dE	$i-z$	interm.	64.87	55.68
dE	$i-z$	large	86.48	52.66

NOTE. — For a given dE subclass (1st column), color (2nd column), and aperture (3rd column), we compare the CMRs of the low and high-density subsamples (see text). Probabilities for a common underlying distribution are derived from a K-S test (4th column) and a Student's t-test for unequal variances (5th column).

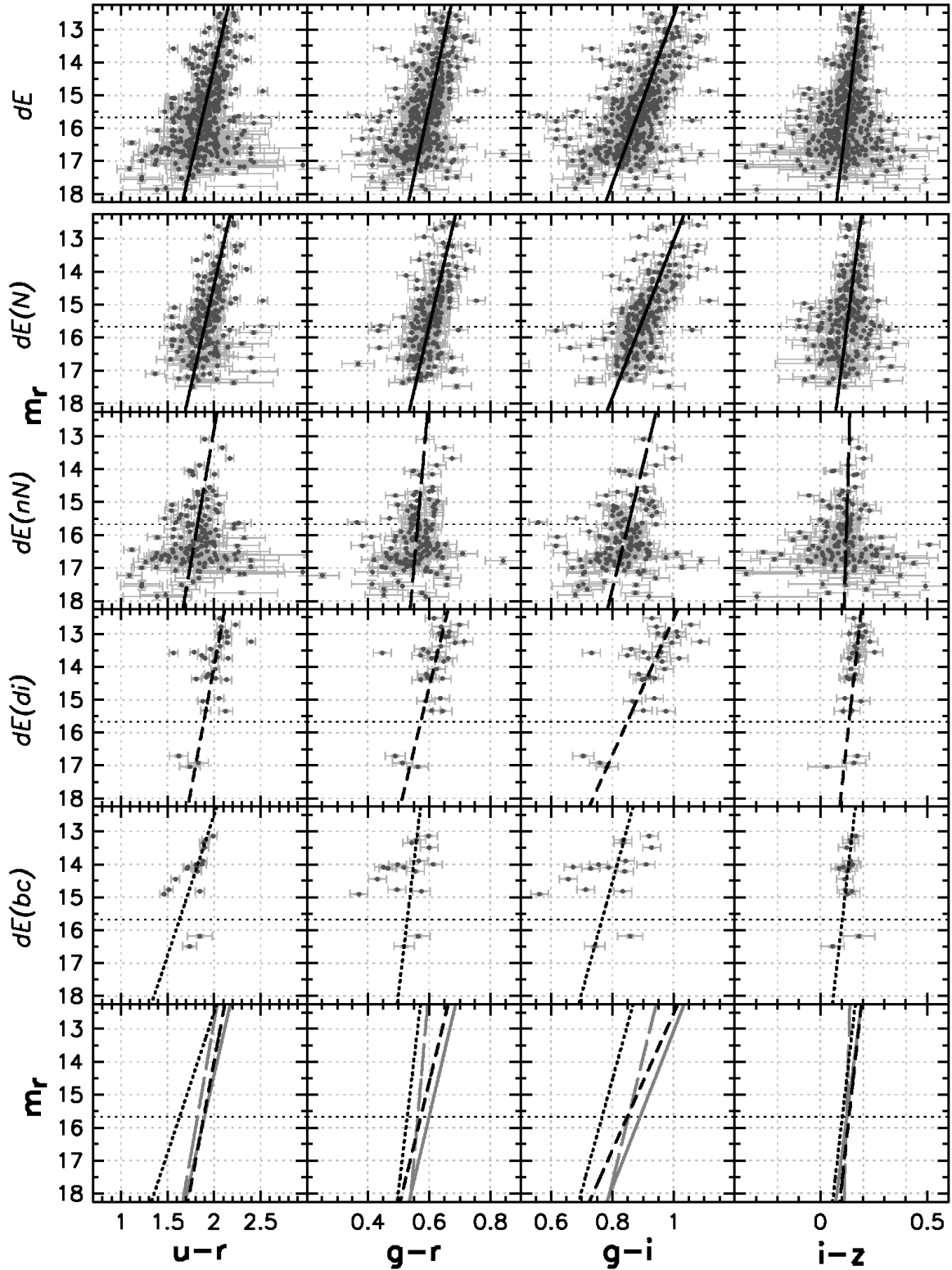


FIG. 1.— Color-magnitude relations of dE subclasses. Shown are the relations of r magnitude with $u-r$, $g-r$, $g-i$, and $i-z$ color for the different dE subclasses (different rows, as labelled on the left-hand side) and the full dE sample excluding dE(bc)s (top row), using the half-light aperture. The linear fits to the CMR of each subclass are shown as lines of different style, and are plotted again in the bottom row for comparison. There, two lines are shown in grey, to allow a better visual distinction. Both color and magnitude errors are shown; however, the latter are in most cases smaller than the size of the data points.

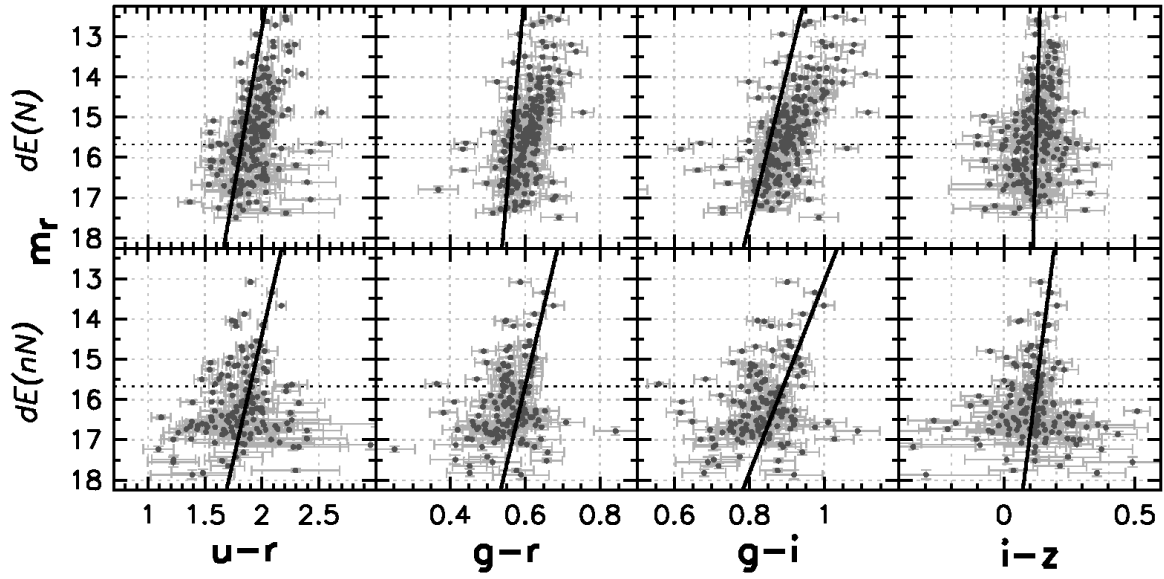


FIG. 2.— Comparison of the CMR of $dE(N)$ s and $dE(nN)$ s. Similar to the second and third row of Figure 1, but now overplotting the fit to the $dE(nN)$ s over the data points of the $dE(N)$ s, and vice versa.

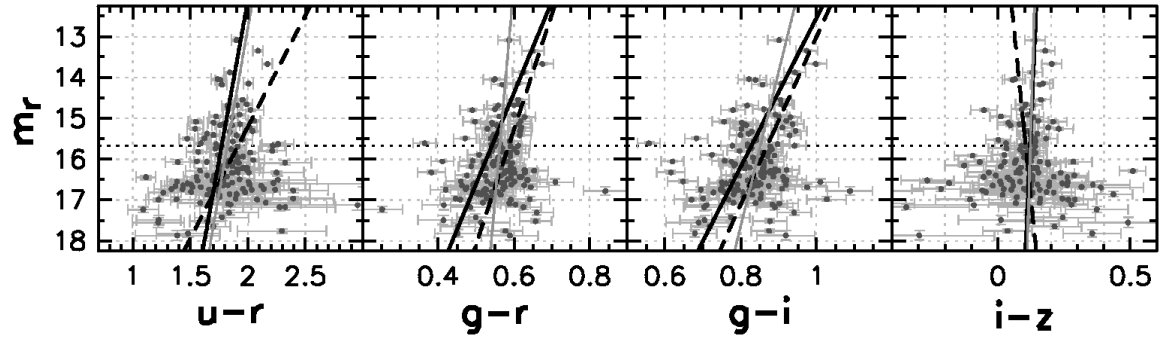


FIG. 3.— Comparison of the CMR of bright and faint $dE(nN)$ s. Similar to the third row of Figure 1, but now showing the fit to the full $dE(nN)$ sample as grey line, the fit to only the bright subsample as black solid line, and the fit to only the faint subsample as black dashed line.

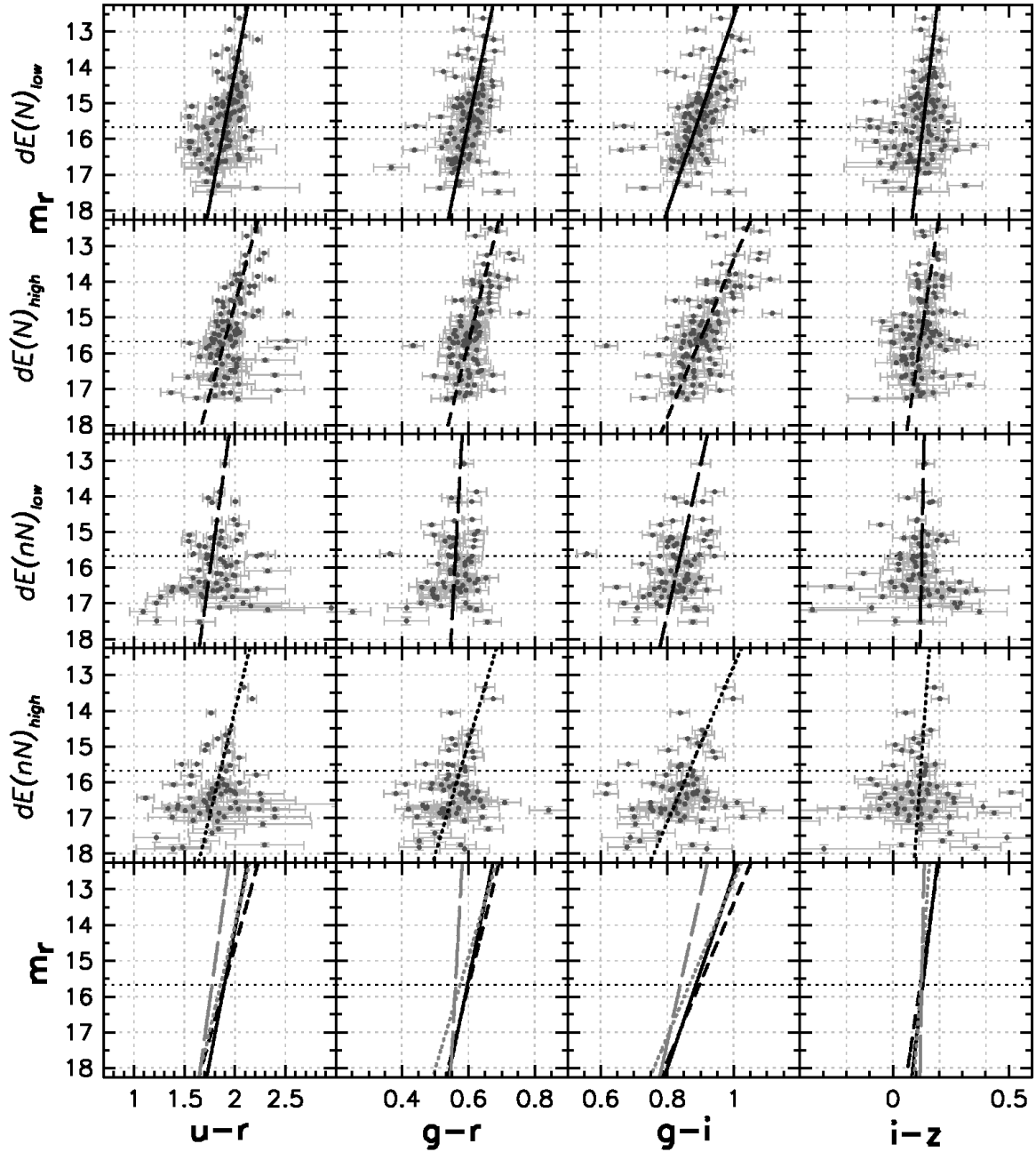


FIG. 4.— Color-magnitude relations for different densities. Similar to Figure 1, but showing the CMR of the low-density and high-density subsamples of the $dE(N)$ s and the $dE(nN)$ s, as labelled on the left-hand side. Again, two of the lines are shown in grey in the bottom row, to allow a better visual distinction.

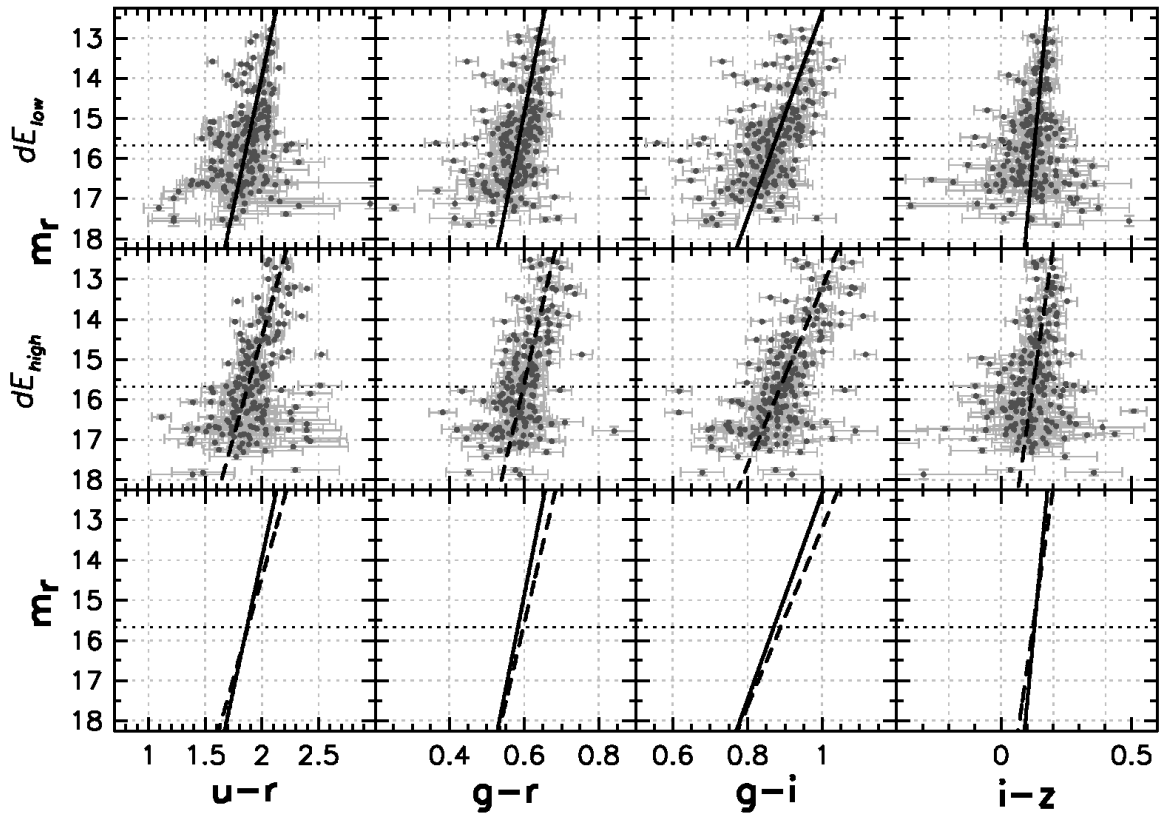


FIG. 5.— Color-magnitude relations for different densities. Same as Figure 4, but for the full dE sample, excluding dE(bc)s.

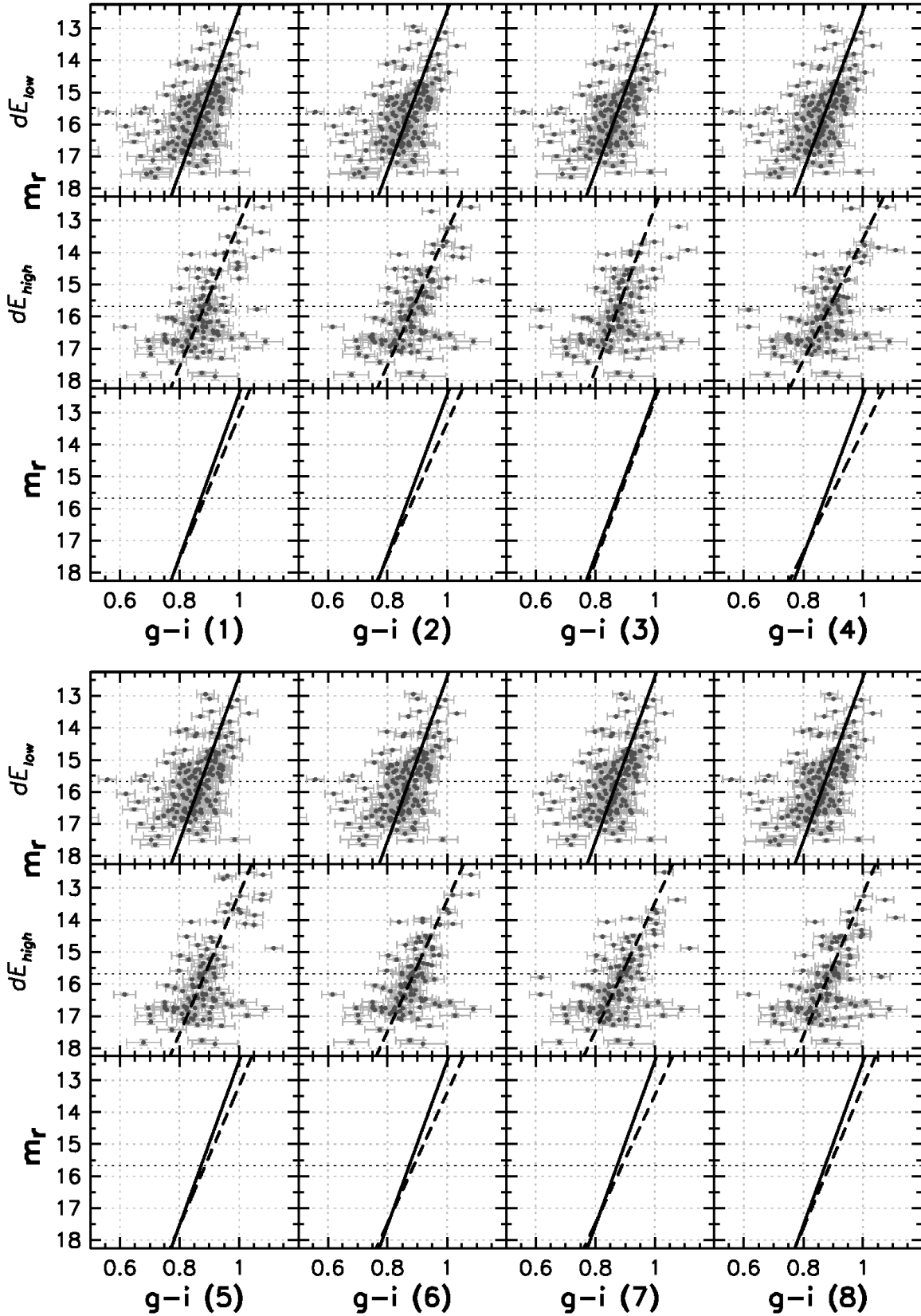


FIG. 6.— Color-magnitude relations for different densities. Similar to Figure 5, but showing the first 8 random realizations of the “combined sample” (see text), which contains equal numbers of $dE(N)$ s and $dE(nN)$ s in both its low- and high-density part. Colors were measured in $g-i$ using the half-light aperture.

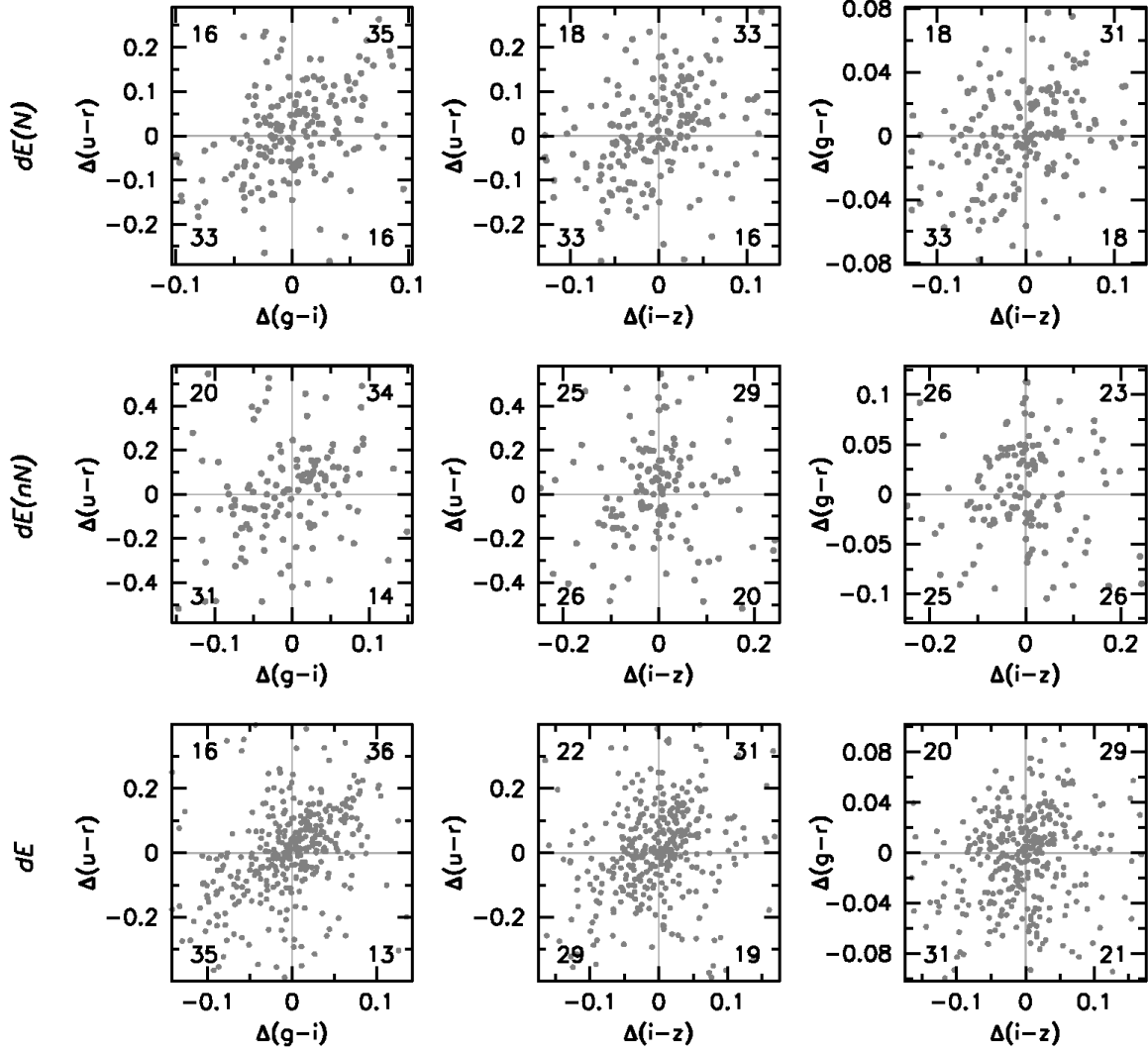


FIG. 7.— Correlation of colors. Pairwise comparison of the color residuals about the respective CMRs, for colors measured within the half-light aperture. For a given galaxy, $\Delta(u-r) := (u-r) - (u-r)_{\text{CMR}}$, where $(u-r)$ is the galaxy's color, and $(u-r)_{\text{CMR}}$ is the color value of the linear fit to the CMR at the r magnitude of the galaxy; same for the other colors. The black numbers in the corners of the diagrams give the percentage of galaxies within the respective quadrant, bordered by the grey lines.

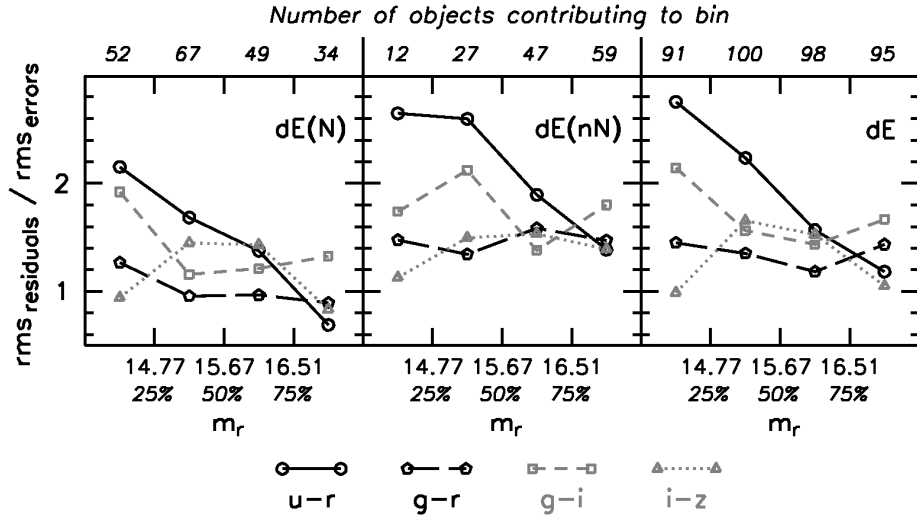


FIG. 8.— Relation of CMR scatter and magnitude for different colors. Shown is the ratio of the rms of the color residuals about the CMR to the rms of the color errors, binned to quartiles defined by the r brightnesses of our full sample. Quartiles are separated at $m_{r,\text{bri.}} = 14.77$, $m_r = 15.67$, and $m_{r,\text{fai.}} = 16.51$ mag (see text) as labelled below each panel; the x-axis thus does not follow a linear scale. Values were derived using the half-light aperture.

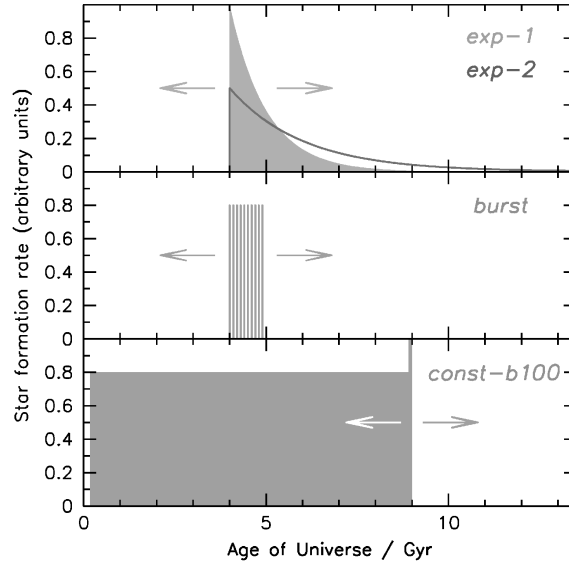


FIG. 9.— Star formation histories. Illustration of the star formation histories used for our population synthesis models. *Top panel:* The *exp* models. *Middle panel:* The *burst* model. *Lower panel:* The *const-b100* model, in which the final burst reaches a SFR of 80 in the units adopted here. See text for details.

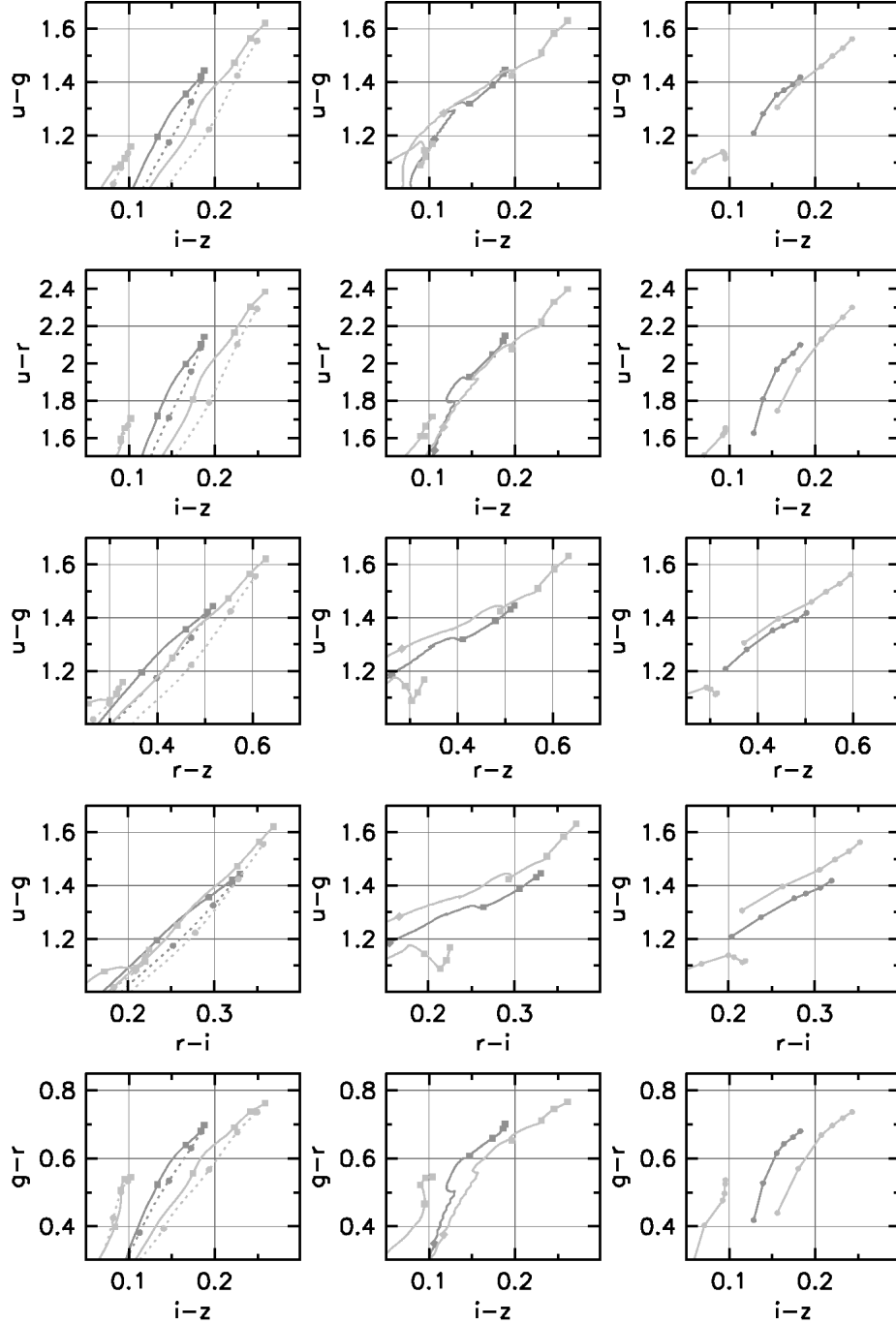


FIG. 10.— Population synthesis models. Shown are theoretical galaxy colors along Bruzual & Charlot model tracks of constant metallicity, namely $Z = 0.008$ ($[\text{Fe}/\text{H}] = -0.33$, rightmost track, light grey), $Z = 0.004$ ($[\text{Fe}/\text{H}] = -0.64$, middle track, dark grey), and $Z = 0.0004$ ($[\text{Fe}/\text{H}] = -1.65$, leftmost track, light grey). The left column shows our *exp* model, i.e., a star formation peak that exponentially declines with a decay time of $\tau = 1$ Gyr (solid lines) and 2 Gyr (dotted lines). The middle column shows our *burst* model, i.e., 10 short bursts of star formation occurring within 1 Gyr. For both the *exp* and the *burst* models, each model track reaches from an age of 1 Gyr (lower end, typically outside the plotting range) to 13.5 Gyr (upper end). Ages are marked at 4.5, 7.5, 10.5, and 13.5 Gyr with filled squares or filled circles (*exp-2* model). For the *burst* model, we give another age mark at 1.5 Gyr (filled diamond). The right column shows our *const-b100* model, i.e., constant star formation that is truncated at a certain epoch, including a final burst (see Figure 9). For this model, the model tracks actually are simply lines that connect the data points for a truncation of star formation that, from bottom to top, occurred 0.5, 1, 2, 3, 5, and 7 Gyr ago.

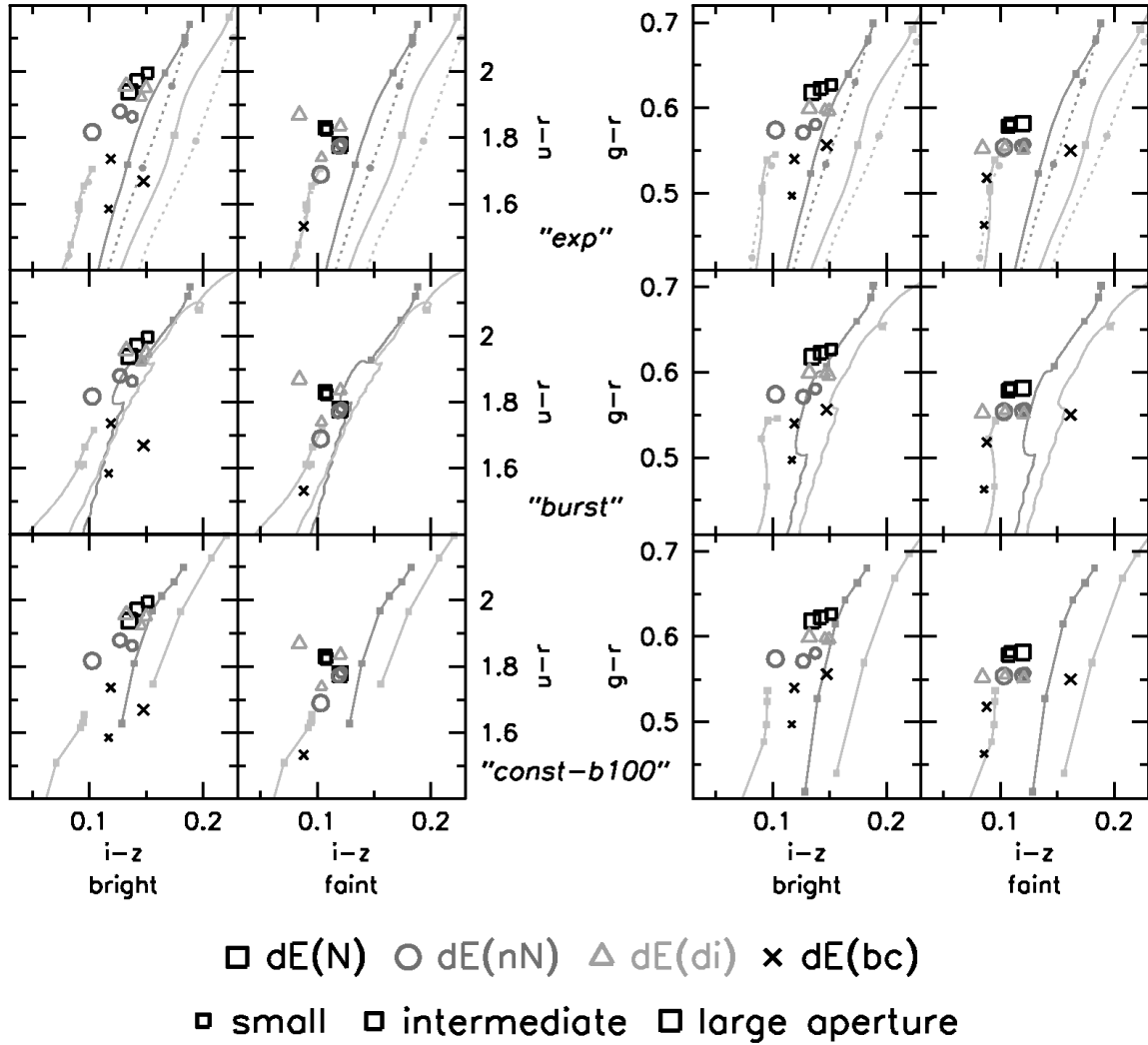


FIG. 11.— Color and stellar population properties of the dE subclasses. Color values of the CMRs of dE(N)s (black squares), dE(nN)s (grey circles), dE(di)s (light grey triangles), and dE(bc)s (black crosses), measured at the bright and faint reference magnitudes, as labelled below the diagrams. Small symbols indicate colors measured within the small aperture, intermediate-size symbols represent the intermediate aperture, and large symbols mark the colors within the large aperture, to illustrate systematic gradients. In the left part of the figure we show $u-r$ vs. $i-z$ diagrams, while $g-r$ vs. $i-z$ diagrams are shown in the right part. Model tracks (as in Figure 10) are shown for the *exp* models (top row), the *burst* model (middle row), and the *const-b100* model (bottom row).

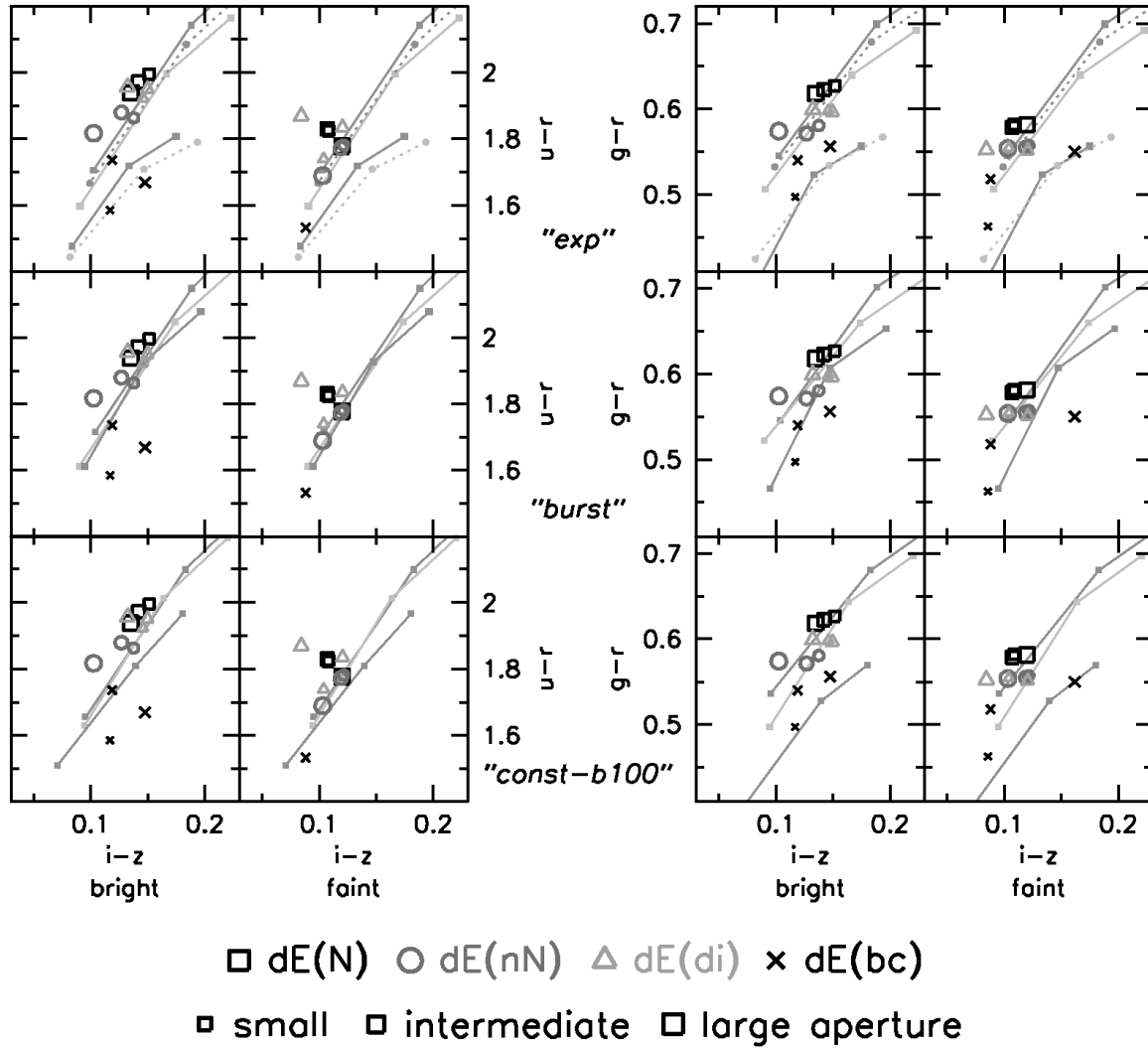


FIG. 12.— Color and stellar population properties of the dE subclasses. Same as Figure 11, but with model tracks now being lines of constant age (instead of constant metallicity). For the *exp* and the *burst* models, the tracks represent ages of 4.5, 7.5, and 13.5 Gyr. For the *const-b100* model, the tracks connect points of constant truncation times, namely 1, 3, and 7 Gyr ago.